Geophysical Journal International

Geophys. J. Int. (2025) **244,** 1–17
Advance Access publication 2025 November 18
Research Paper

https://doi.org/10.1093/gji/ggaf468

Inference of the *S*- to *P*-wave velocity anomalies ratio and its uncertainty with an application to South-East Asia

Emile Serra [1], Christophe Zaroli [1], Sophie Lambotte[1] and Paula Koelemeijer [2]

[1] *Institut Terre et Environnement de Strasbourg, Université de Strasbourg, EOST, CNRS, UMR 7063, 5 rue Descartes, F-67084 Strasbourg, France. E-mail: emile.serra@unistra.fr*

[2] *Department of Earth Sciences, University of Oxford, Oxford OX1 3AN, United Kingdom*

Accepted 2025 November 11. Received 2025 October 10; in original form 2025 May 27

SUMMARY

The ratio R of shear-wave to compressional-wave velocity variations ($\mathrm{d}\ln V_s/\mathrm{d}\ln V_p$) is a useful physical parameter to study the thermochemical properties of the Earth's interior. Several approaches have been employed to estimate R (or its inverse $1/R$), but they either assume the same local resolution in models of $\mathrm{d}\ln V_s$ and $\mathrm{d}\ln V_p$ or assume the same ray paths for *S*- and *P*-phases, while excluding valuable data and overlooking uncertainties. We overcome these issues by characterizing both $\mathrm{d}\ln V_s$ and $\mathrm{d}\ln V_p$ through the Backus-Gilbert based subtractive optimally localized averages (SOLA) method to obtain R including its uncertainties. This approach enables us to ensure that $\mathrm{d}\ln V_s$ and $\mathrm{d}\ln V_p$ share the same local resolution, making it possible to compute their ratio through division. In addition, SOLA provides uncertainties on $\mathrm{d}\ln V_s$ and $\mathrm{d}\ln V_p$, which we propagate into our estimates of R using the Hinkley distribution for $\mathrm{d}\ln V_s/\mathrm{d}\ln V_p$. When resembling a Gaussian, the Hinkley distribution provides Gaussian uncertainties for R, enabling us to interpret tomographic features as, for instance, in terms of slab morphology or partial melt with greater confidence. To illustrate our new approach, we use a data set of *P*- and *S*-phase onset-time residuals from ISC to infer the velocity anomalies and the ratio R (or $1/R$) in South-East Asia between 100 and 800 km depth. As the SOLA method is driven by data uncertainties, we reassess the provided ISC uncertainties using a statistical approach before developing models of $\mathrm{d}\ln V_s$ and $\mathrm{d}\ln V_p$ with their uncertainties. Based on our quantitative model estimates, we argue that a large velocity anomaly below the Sumatra slab, with a value of R over 2.5, is resolved given our data and their uncertainties. However, in contrast to previous work, we do not find evidence for a slab hole under Java. Our proposed approach to obtain R with uncertainties using the Hinkley distribution can be applied to a large range of tomographic imaging settings.

Key words: Inverse theory; Body waves; Seismic tomography; Subduction zone processes.

1 INTRODUCTION

Seismic tomography is an essential tool to understand the interior of the Earth, from its surface to depths that we would never be able to access physically (Aki *et al.* 1977). Thanks to our knowledge of compressional- (V_p) and shear-wave (V_s) velocities through rock physics and seismology, we are able to test hypotheses about the structures composing the Earth's interior (e.g. Crossley 1997; Karato *et al.* 2000; Nolet 2008; Ritsema & Lekić 2020; Toyokuni *et al.* 2022; Fichtner *et al.* 2024). Ideally, multiple physical parameters may be jointly interpreted, as this is more effective for constraining the potential responsible physical phenomena in a quantitative manner. Indeed, V_p is sensitive to the bulk modulus, shear modulus and density, while V_s is only sensitive to the shear modulus and density. In this context, comparing the two provides insight into the relative behaviour of these material properties (e.g. Masters *et al.* 2000; Gercek 2007). By examining their difference, the V_p/V_s ratio provides useful information on the thermochemical structure of the Earth's interior (e.g. Karato 1993; Masters *et al.* 2000; Hernlund & Houser 2008). The absolute V_p/V_s ratio is mostly used in studies of the crust (e.g. Hamada 2004; Aryanti *et al.* 2018), whereas other related ratios, such as $R = \mathrm{d}\ln V_s/\mathrm{d}\ln V_p$, the inverse ratio of relative velocity anomalies, are preferentially investigated in studies of the deep mantle (e.g. Masters *et al.* 2000; Koelemeijer *et al.* 2015; Tesoniero *et al.* 2016; Restelli *et al.* 2024). For example, the V_p/V_s ratio has been employed to unveil traces of liquid, such as partial melting under volcanoes (e.g. Aryanti *et al.* 2018), in subduction zones and ridges (e.g. Conder & Wiens 2006; Reyners *et al.* 2006; Audet & Bürgmann 2014). Traces of liquid water saturation can also be detected near subducted slabs (e.g. Hyndman & Peacock

2003), or in geothermal contexts (e.g. Mahartha *et al.* 2019). This ratio may help to discriminate between hot, altered or fractured rocks (e.g. Aryanti *et al.* 2018), while it is also used in the oil and gas industry to discover and monitor hydrocarbons pockets (e.g. Hamada 2004). In the lower crust, seismic velocities have been analysed to estimate the volume of serpentinization and the quartz volume that may be trapped under the crust by rising fluids (e.g. Ramachandran & Hyndman 2012). At greater depths, the ratio R is thought to indicate chemical variations and/or phase transitions in the mantle, for example in the mid-mantle where the spin crossover in ferropericlase occurs (e.g. Shephard *et al.* 2021; Trautner *et al.* 2023; Cobden *et al.* 2024). Furthermore, Gerya *et al.* (2006) among others suggested that variations in R may be used to distinguish between different subduction-related plumes that lead to a chemical difference in the magma. In the lowermost mantle, variations in R, possibly due to the phase transition of bridgmanite to post-perovskite or the chemical composition of the large-low-velocity provinces, remain the matter of debate (e.g. Hernlund & Houser 2008; Davies *et al.* 2015; Koelemeijer *et al.* 2018; Leung *et al.* 2025). Finally, the ultra-low-velocity-zones (ULVZs), which have been observed on top of the core–mantle boundary, might be due to chemically distinct, dense material (e.g. Rost 2013; McNamara 2019). Robust constraints on their R value would provide insights into their cause (chemical or partial melt). The above examples indicate that our ability to accurately constrain the V_p/V_s ratio and its variants (e.g. R) is useful in many different applications aimed at deciphering the Earth's interior, all the way down to the lowermost mantle.

In these studies, two main methods are usually employed to infer ratios between seismic velocities: the *direct* and the *division* method. For the direct method, the differential ratio $\mathrm{dln}\left(V_p/V_s\right)$ is inverted for, sometimes jointly with $\mathrm{dln}V_p$, using differential S–P arrival times (e.g. Walck 1988; Zenonos *et al.* 2020). For the division method, models for both $\mathrm{dln}V_p$ and $\mathrm{dln}V_s$ are obtained, and then divided 'cell by cell' (e.g. Masters *et al.* 2000; Tesoniero *et al.* 2016; Calò & Tramelli 2018; Zenonos *et al.* 2020). However, each approach comes with its own drawbacks. For the direct method, one supposes the same P and S ray path sensitivities in a reference Earth model. This is often inherently incorrect as the ray paths are only identical when the V_p/V_s ratio of the reference model is constant and when the frequency content of the waves is also considered (e.g. Chaves *et al.* 2020). It also requires to have successfully measured both P and S arrival times for each source–receiver pair, thus potentially discarding valuable individual P or S data. When using the division method, we assume the local resolution of the $\mathrm{dln}V_p$ and $\mathrm{dln}V_s$ models to be the same, which is not guaranteed and typically not the case (e.g. Eberhart-Phillips 1990; Hernlund & Houser 2008). Determining velocity anomalies on its own is not sufficient for further robust geophysical interpretations. Resolution and uncertainty are also required to assess the reliability of tomographic models: resolution indicates which structures can be tomographically imaged given the ray coverage, while uncertainty quantifies how strongly the data support those structures (e.g. Rawlinson *et al.* 2014; Fichtner *et al.* 2024). Traditional inversion methods, such as those based on damped least squares (DLS) inversions, do not easily provide this crucial information, especially when dealing with large-scale inverse problems (e.g. Nolet 2008; Fichtner *et al.* 2024). Some probabilistic tomography studies have considered uncertainties on the ratio R, particularly in the deep mantle (e.g. Resovsky & Trampert 2003; Trampert *et al.* 2004; Mosca *et al.* 2012), but these studies do not provide direct resolution information. Until recently (Restelli *et al.* 2024), there has been, to the best of our knowledge, no study that formally assessed both the uncertainties and the resolution of the ratios of seismically constrained parameters (such as $R = \frac{\mathrm{dln}V_s}{\mathrm{dln}V_p}$) in the case of the division method. Erroneous ratios may arise when directly dividing cell-by-cell $\mathrm{dln}V_p$ and $\mathrm{dln}V_s$ estimates without taking this into account. To mitigate this, different approaches have been developed in previous studies. For example, Hernlund & Houser (2008) used the R_σ metric, which compares the dominant features of the $\mathrm{dln}V_p$ and $\mathrm{dln}V_s$ distributions at each depth and thus avoids dependence on poorly constrained values. Alternatively, some studies have analysed the depth-dependence of the ratio by dividing the RMS value of $\mathrm{dln}V_s$ and $\mathrm{dln}V_p$ (e.g. Koelemeijer *et al.* 2015; Tesoniero *et al.* 2016). The need to further include model uncertainties and similar resolution in efforts to obtain R motivates this work.

We present a new method for inferring the ratio $R = \mathrm{dln}V_s/\mathrm{dln}V_p$ (or $1/R$) in a robust manner, along with information on its corresponding resolution and uncertainty, by taking advantage of the division method with (i) the subtractive optimally localized averages (SOLA)–Backus-Gilbert inversion and (ii) the Hinkley probability density distribution. For this purpose, we use the SOLA method, which was initially developed for 1-D helioseismic inversions by Pijpers & Thompson (1992, 1993) and introduced to seismic tomography by Zaroli (2016, 2019). Thanks to it, we can build a pair of unbiased models for $\mathrm{dln}V_p$ and $\mathrm{dln}V_s$ (Zaroli *et al.* 2017), imposing equal local resolution (Restelli *et al.* 2024) and estimating their uncertainties (e.g. Latallerie *et al.* 2022, 2025; Amiri *et al.* 2023; Freissler *et al.* 2024; Mag *et al.* 2025). Therefore, where the resolution is comparable, the division is physically meaningful. Indeed, a local *a priori* resolution can be specified by the user through the target kernels, which represent the resolution we aim to achieve locally, as well as a trade-off parameter that balances the fit to the target kernel with the model uncertainties. With SOLA, the local resolution represents the volume over which the average of the unknown 'true' velocity anomalies is computed, along with its associated Gaussian uncertainty. We can therefore take full advantage of the division method by keeping all available, even unpaired, P and S data. This should in principle lead to a better resolution and lower uncertainties (e.g. Eberhart-Phillips 1990; Liu *et al.* 2023). Instead of simply keeping paths that have both P and S arrival times (e.g. Kennett *et al.* 1998; Gorbatov & Kennett 2003), our SOLA-based strategy allows us to maximize the similarity in resolution between the $\mathrm{dln}V_p$ and $\mathrm{dln}V_s$ models, enabling a more meaningful computation of the ratios. In addition, traditional inversion methods (such as DLS) invert for all model parameters at once. To dampen the effect of incomplete and noisy data, especially in areas with sparse data coverage, model regularization needs to be applied, which impacts the recovered solution also in regions of interest. To reduce this effect, many regional studies only keep ray paths that are fully restricted to the area of interest (e.g. Zenonos *et al.* 2019). This greatly restricts the use of data partially outside the studied zone, hence potentially limiting the resolution of the P and S models, especially at deeper mantle depths. Yet, this is not a problem with SOLA, since by construction a model consists of a collection of independently estimated local averages. It is straightforward to deal with both regional and teleseismic data, and to only focus on the enquiry points of interest, within the study region. Consequently, with the knowledge of $\mathrm{dln}V_p$ and $\mathrm{dln}V_s$ Gaussian uncertainties provided by SOLA, the division process now involves four parameters: instead of just dividing the velocity anomalies, we must divide two Gaussian distributions. The analytic formula of the probability density function (PDF) resulting from this division is

given by the Hinkley distribution (Hinkley 1969). While this distribution is used in other fields (e.g. Ruggieri *et al.* 2011; Lennox *et al.* 2012; Dhanoa *et al.* 2018), to the best of our knowledge, this study is the first to formally take advantage of the Hinkley distribution for inferring the ratio R and its uncertainty in seismic tomography.

As a test application of our method, we focus on the South-East Asia region (SE Asia) between 100 and 800 km depth, using ISC traveltime data within the framework of ray theory, because of its geological and structural diversity (see e.g. fig. 1 of Hutchings & Mooney 2021). Most existing tomographic studies of SE Asia have focused on the *P*-wave structure (e.g. Widiyantoro *et al.* 2011; Hall & Spakman 2015; Huang *et al.* 2015; Zenonos *et al.* 2019; Toyokuni *et al.* 2022; Wang *et al.* 2022; Xie *et al.* 2023). Some of these have identified a possible hole under Java in the subducting slab, just below the Madura strait, extending from 280 to 430 km depth (e.g. Widiyantoro *et al.* 2011; Hall & Spakman 2015; Zenonos *et al.* 2019; Toyokuni *et al.* 2022; Wang *et al.* 2022; Xie *et al.* 2023). Moreover, some studies have claimed to image a Subslab Hot Mantle Upwelling (SHMU) (Toyokuni *et al.* 2022), and Subslab Low Velocity Anomaly (SLVA) (Fan & Zhao 2021) below the Sumatra slab that may extend down to over 1500 km. This structure, characterized by large low velocity anomalies (about −1 per cent) for *P* (Toyokuni *et al.* 2022), located below the slab, is also present in other tomographic studies, even though they have not specifically interpreted it (e.g. Hall & Spakman 2015; Wang *et al.* 2022). There are also some local and shallow *P* and *S* tomographic studies that aimed to study the volcanoes of the region (e.g. Okabe *et al.* 2004; Rosalia *et al.* 2019; Liu *et al.* 2021; Silitonga *et al.* 2023). Unfortunately, these only probe the Earth's interior down to 100 km depth, which is shallower than the scope of this study. Some regional *S*-wave studies, such as Zenonos *et al.* (2019) and Wehner *et al.* (2022), and numerous global *S*-wave studies exist (e.g. Montelli *et al.* 2006; Koelemeijer *et al.* 2015; Tesoniero *et al.* 2015; Zaroli 2016; Durand *et al.* 2017; Lu *et al.* 2019), though their resolution, if estimated, is usually not as good as for regional studies, and their uncertainties are barely known. Directly relevant to this work is the study by Zenonos *et al.* (2020), who compared the seismic velocity ratios obtained from the division and direct methods. However, they performed no assessment of uncertainties, and their resolution analysis was qualitative. They concluded that the division method does not provide satisfactory results because of a too high dependence on the produced 3-D *S*-wave model. However, they did not discuss the difference in resolution and uncertainty between the *P* and *S*-wave tomography models. We shall explicitly investigate this with our new methodology, and discuss the value of the division method when obtained following our approach.

In Section 2, we present how we build our data set for SE Asia, which consists of *P*- and *S*-wave onset-time traveltime residuals from the International Seismological Center (ISC), and we explain how we reassess their uncertainties given these are crucial for SOLA. In Section 3, we explain our new method for inferring the ratio R and its uncertainty. This is based on the division of two SOLA-based tomographic models of comparable resolution for both $\mathrm{d}\ln V_p$ and $\mathrm{d}\ln V_s$, with their (Gaussian) uncertainties taken into account in the Hinkley-based division process. In Sections 4 and 5, we present the results of our method when applied to SE Asia in the 100–800 km depth range, as well as further discussion.

2 DATA

In the following, we describe how we build our data set, with their uncertainties, which will serve as inputs for our SOLA-based tomographic inversion. In this study, we will utilize the ray-theoretical framework for simplicity. We first select body-wave traveltime residuals from data sets of the International Seismological Centre (ISC), in order to study the SE Asia region between −5○ and 13○ latitude and between 95○ and 130○ longitude, from the Earth's surface down to 800 km depth. We subsequently regroup these data into summary rays, which enables us to reassess their uncertainties. Additionally, we apply a crustal correction, since this is not included in the ISC data.

2.1 Data selection from the ISC-EHB and ISC-reviewed data sets

We select onset-time residuals of direct phases (*P*, *S*) and their depth phases (pP, sS). As recently discussed by Nolet (2023), PP and SS phases may be affected by a huge bias, because they are often picked late in the presence of noise and we therefore do not include them in this study. Other phases could be used, but for simplicity and to restrict the total number of data, we limit ourselves to these four phases (*P*, *S*, pP and sS). We use a mix of two ISC data sets: the ISC-Reviewed ('ISC-Rev', International Seismological Centre 2023a), and the ISC-EHB ('EHB', International Seismological Centre 2023b). The latter is of better quality since a relocation procedure was applied to each event (Engdahl *et al.* 1998, 2020; Weston *et al.* 2018). Specifically, we extract data from the entire EHB data set, between 1964 and 2019, but this unfortunately lacks data for the sS phase. Thus, we add these data using the recent ISC-Rev data set, between 2002 and 2019. While both data sets have been entirely 'reviewed', only the EHB data set has been explicitly relocated for events after 1964. Thus, we decide to only keep recent data (since 2002) from the ISC-Rev data set to ensure a similar overall quality in our data set. If an event is present in both the EHB and ISC-Rev selected data subsets, we fix the event location according to the EHB catalogue, and recompute the corresponding traveltime residuals for the sS depth phase, using the ISCLOC software (see Bondár & Storchak 2011) for consistency. We do not take uncertainties in the source into account, but their effects are accounted for by using summary rays (see below). From these data sets, we only keep data with ray paths crossing the larger SE Asia region of interest [see the black box in Fig. 1(a)]. Nolet & van der Lee (2022) recomputed data uncertainties of two subsets of ISC *P*-wave data, the first containing all data, and the second being composed of data with pick uncertainties lower than 0.1 s. They found that the second subset resulted in smaller data uncertainties. We assume that a similar outcome is to be expected for all phases. Consequently, our data set is only composed of data with pick uncertainties lower than 0.1 s. To avoid issues due to phase triplications, we only keep data in epicentral distances ranges of 29°–96° for *P* and 28°–97° for *S*. These intervals are similar to those used by Lei & Zhao (2006) and Hosseini *et al.* (2019). For the pP and sS depth phases, due to additional complexity in the associated triplications, we also define a minimal epicentral distance based on each event's depth, to retain as many depth phases as possible. For pP, we set the minimal epicentral distance to 30°, 32°, 35°, 38°, 40°, 42° and 43°, respectively for event depths lower than 200, 350, 500, 550, 600, 650 and 700 km, while we always keep a maximal epicentral distance of 96°.

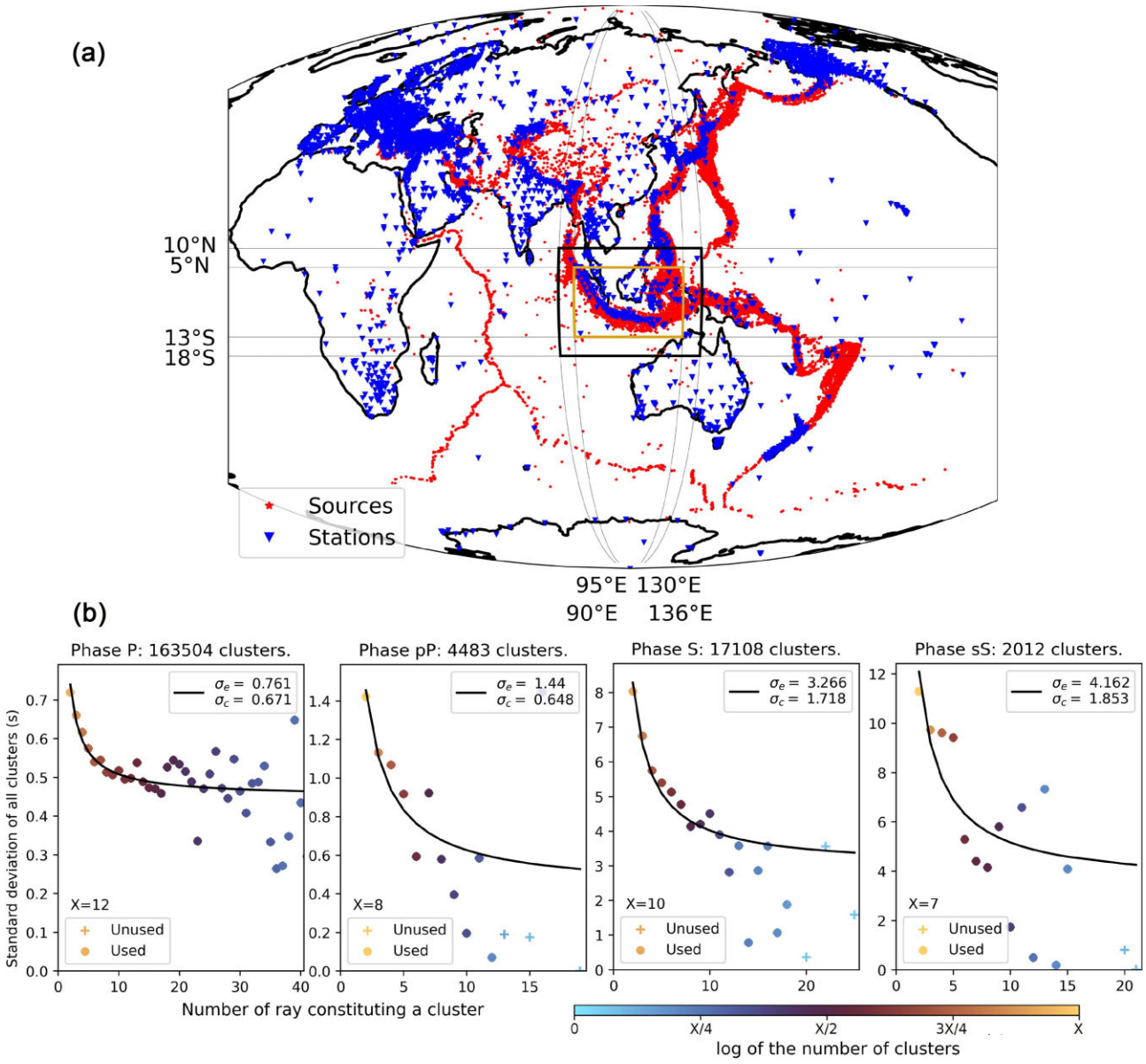

Figure 1. Details of the data used in this study. (a) Map of sources (red stars) and receivers (blue triangles). Source locations correspond to the barycentre of each summary ray. We select data that sample the large black box around South-East Asia. To avoid any border effects, we only perform the SOLA inversion and interpret results in the smaller, yellow, rectangular region. (b) Data uncertainties estimated using the method by Morelli & Dziewonski (1987) and Nolet (2023). For each phase, we represent the Morelli-Dziewonski fit, $f(\sigma_E, \sigma_C)$, for summary rays (SR) related to crustal events only. For the *P* phase, we show example data for the lower mantle range. Plus symbols represent groups of SRs not used in the fitting procedure, contrarily to circles. The higher the log of the number of SRs (X) used in the computation of $\sigma_N^2(N)$, the more weight they are given in the fit. See Section 2.4 for the definition of σ_e, σ_c and σ_N.

For the sS phase, we fix the minimal epicentral distance at 31°, 34°, 37°, 39°, 40° and 41°, respectively for event depths lower than 150, 180, 550, 600, 620 and 700 km, each with a maximal distance of 97○. It results in a total of 3922 340 P, 223 006 S, 120 045 pP and 27 840 sS onset-time residuals.

2.2 Summary rays

In order to reduce the number of data while retaining all information contained in the data, we group adjacent rays into summary rays (SR) (e.g. Nolet 2023). To build the SRs, we group rays departing from all sources contained in a cube of size 30×30×30 km^3 towards the same receiver. To remove the outliers within each SR, we define two types of outliers: spatial and temporal. We consider these separately as the different rays could be travelling through slightly different structures, thus leading to significant differences in the time domain. In this case, these anomalous data should not be removed as they still yield precious information on 3-D Earth structure. To detect spatial outliers, we make use of the DBSCAN algorithm (Ester *et al.* 1996) based on the spatial coordinates of the sources. Temporal outliers are identified by combining the Double MAD and Dixon-Q tests, applied to the traveltime residuals. The Dixon-Q test (Dixon 1950) is particularly efficient for finding singular outliers in small distributions. Following Rorabacher (1991), who improved Dixon's method, we develop an algorithm that can detect 0 to 4 outliers in a small distribution containing up to 20

members. However, Dixon's test works poorly when the temporal distribution is too narrow. We therefore also test whether the difference between the two most extreme values is larger than twice the phase uncertainty estimated by Bolton & Masters (2001), that is, 1.27 and 2.38 s for *P* and *S* phases, respectively. For more populated distributions, we successfully detect temporal outliers using a Double MAD algorithm (Leys *et al.* 2013). Having found both spatial and temporal outliers, each class identified by DBSCAN is closely inspected: if all the elements are temporal outliers, they are kept and regrouped as a separate SR. Otherwise, temporal outliers are simply discarded. Spatial outliers that are not temporal outliers are kept within the SR. Finally, the SR source location is computed as the barycentre of all the sources composing the SR, and the corresponding time residual is computed as the mean of all associated data. The procedure described above has resulted in 2 149 360 P, 169 690 S, 94 317 pP and 19 319 sS summary rays.

2.3 Crustal corrections

In our ray-theoretical framework, we assume that crustal corrections (CC) for the ISC data only depend on the ray path in the crust. We use the $1\circ \times 1\circ$ crustal model CRUST1.0 (Laske *et al.* 2013) to compute the corrections. Having most of our data located between 60°S and 60°N, where 1° longitude is larger than 60 km, CRUST1.0 patches are at least six times larger than the SR discretization, and up to 11 times larger near the equator. Therefore, we decide to only compute the crustal correction for the SR, and not for all rays composing each SR, as most of the rays likely lead to the same correction. We compute the CC using the algorithm `raydyntrace` of Tian *et al.* (2007), using CRUST1.0 and the 1-D reference model AK135 (Kennett *et al.* 1995) for consistency with the ISC data set. We discard data for which the CC could not be computed, which is mostly due to phase incompatibilities when adding the CRUST1.0 model and occurs primarily for rays too close to the bounds of the considered epicentral distances. These incompatibilities only represent less than 0.447 per cent of the original *P* data set, and less than 2.821 per cent of the *S* data set.

2.4 Reassessment of ISC data uncertainties

Using a new diagnostic approach, Nolet & van der Lee (2022) and Nolet (2023) concluded that data uncertainties reported in the ISC catalogue appear underestimated overall, and proposed that they can be reassessed using the Morelli & Dziewonski (1987) method. The principle of the Morelli-Dziewonski algorithm is that the variance σ_N^2 of all SR residuals, being composed of N rays, should be written as $\sigma_N^2 = \frac{\sigma_E^2}{N} + \sigma_C^2$, with σ_E the uncertainty of the data to be estimated (e.g. due to the measurement process, source mislocation, etc.) and σ_C the uncertainty of the SR itself, provided that the locations of all the rays composing the SR are slightly different.

Here, we follow this approach and assume that data uncertainties (σ_E) merely represent standard deviations of Gaussian distributions. In practice, to estimate these uncertainties (σ_E), we group the SRs composed of N rays, compute the variance (σ_N^2) of each group, and find the values of σ_E and σ_C for the function $f(\sigma_E, \sigma_C) = \frac{\sigma_E^2}{N} + \sigma_C^2$ that best fits the points $\sigma_N^2(N)$ (Fig. 1b). For all four seismic phases, we weigh the fitting function f with the log of the number of SRs with N rays, as the fit is more reliable when $\sigma_N^2(N)$ is computed in larger groups of SRs, thus usually for a small N. We only use groups with at least four SRs. Moreover, we subdivide the residuals of each seismic phase as a function of the event depth to separate events occurring in the crust (shallower than 40 km) or in the mantle (deeper than 40 km), since data associated with deep earthquakes are expected to be less uncertain due to sharper onsets (Nolet & van der Lee 2022). We further divide the *P* phase data, as they are more numerous, based on the depth of the SR's turning point into the following ranges: 600–1200, 1200–2600 and 2600–2891 km, respectively representing the mid, lower and lowermost mantle. As a remark, our data set does not contain SR with turning points shallower than 600 km depth. We remove outliers by removing any data with residuals larger than three times the standard deviation of the median values for the phase from our final data set.

We note that there could be other sources of uncertainties not taken into account in this work, such as uncertainties in the source parameters or a systematic bias related to the inaccuracy of the crustal model used to compute the crustal correction. Rays from a particular SR could also be sampling different cells of the crustal model compared to our $30 \times 30 \times 30$ km^3 discretization cubes, while we consider all rays of the SR to have the same CC. To estimate the effect of this, one could look at the CC obtained using different crustal models. Moreover, there might be additional uncertainties related to the focal mechanism, but we expect these to be weak when dealing with onset-time residuals, as these are only weakly sensitive to source complexities. Finally, there may be an influence from radial and azimuthal anisotropy and attenuation, but we also expect these to have a small effect on onset-times. To take these additional sources of uncertainty into account in an informal way, we could deliberately inflate our data uncertainties by some percentage (e.g. Latallerie *et al.* 2025). This is what we indirectly do by investigating the sensitivity of the ratio R to a small change in the estimated data uncertainties (see Section 4.2).

To reduce the computational cost of the inversion, we only keep SRs composed of at least 2 rays for the more numerous *P* phase data set, while we keep all data for pP, *S* and sS. Our final data set is thus composed of 574 009 *P*, 166 892 *S*, 85 838 pP and 17 513 sS residuals (Fig. 1a), with their reassessed uncertainties, which are used directly in the SOLA inversions. Note that if we had kept only non-unique *P* and *S* data for the same source–event combination, as required by the direct inversion method, our final data set would only have contained around 160 000 couples for *P*/*S* residuals and 5000 for pP/sS. Using our procedure, we have thus gained a significant number of data, 18 000 for *S* phases, and 494 000 for *P* phases.

3 METHODS

In the following sections, we explain how we proceed to invert the data set we have constructed with the reassessed uncertainties in three steps: (1) performing discrete SOLA inversions (Zaroli 2016) of both *P* and *S* data subsets; (2) determining where the *P* and *S* local resolution is comparable using three similarity metrics; (3) utilizing the Hinkley-based division of $\mathrm{d}\ln V_p$ and $\mathrm{d}\ln V_s$ model estimates (if their resolution is similar) and inferring the ratio R with its corresponding uncertainty, provided that Hinkley is Gaussian-like.

3.1 SOLA tomography setup

A main advantage of SOLA is that it produces the uncertainty and resolution of the model estimate in each cell (i.e. each enquiry point), with some control over the resolution we aim to achieve through the use of target kernels (Zaroli 2016). Indeed, SOLA calculates the local average of the computed parameters around the

target cell (for $\mathrm{dln}V_p$ and $\mathrm{dln}V_s$). That is, it finds N generalized-inverse coefficients $x_i^{(k)}$, i being the i-th data and N the number of (P or S) data. For each enquiry point k, those coefficients minimize the misfit between the local resolution, or averaging kernels ($A^{(k)}$ when considering the enquiry point k), of the model and some user-defined *a priori* resolution, or target kernels (similarly, $T^{(k)}$). The trade-off with the output model uncertainty is represented by the trade-off parameter η (eq. 1). Mathematically, this corresponds to (Zaroli 2016):

$$\begin{aligned} &\underset{\mathbf{x}^{(k)}\in\mathbb{R}^N}{\arg\min} \left\{ \sum_{j=1}^{M} V_j \left(A_j^{(k)} - T_j^{(k)}\right)^2 + \left(\eta^{(k)}\right)^2 \sigma^2_{\hat{m}^{(k)}} \right\} , \\ &\text{subject to } \sum_{j=1}^{M} V_j A_j^{(k)} = 1 , \end{aligned} \tag{1}$$

with V_j the volume of the j-th cell and M the number of cells in the tomographic grid. At each enquiry point k, $A_j^{(k)}$ and $\sigma_{\hat{m}^{(k)}}$ are the M values of the averaging kernel and uncertainty of the output model. They depend on the N generalized-inverse coefficients $x_i^{(k)}$:

$$\begin{aligned} A_j^{(k)} &= \tfrac{1}{V_j} \textstyle\sum_{i=1}^{N} x_i^{(k)} G_{ij} , \\ \sigma_{\hat{m}^{(k)}} &= \sqrt{\textstyle\sum_{i=1}^{N} \left(x_i^{(k)} \sigma_{d_i}\right)^2} , \end{aligned} \tag{2}$$

where σ_{d_i} denotes the uncertainty of the i-th datum. Each row of the matrix $\boldsymbol{G}$ contains the projection of the sensitivity onto the tomographic grid, in this case the ray-theoretical sensitivity. To quantify how close the resolving kernels resemble the target kernels, we define the resolution misfit, RM, as (Zaroli 2016):

$$\mathrm{RM} = \sum_{j=1}^{M} V_j \left(A_j^{(k)} - T_j^{(k)}\right)^2 . \tag{3}$$

SOLA's resolution-uncertainty trade-off is influenced by the density of data. For instance, in a data-sparse area, we typically do not have enough information to allow for a small uncertainty. Because of its trade-off with the resolution misfit (RM, see eq. 3), a small value of η will force a small RM, thus increasing the uncertainty, while a large value of η will lead to a larger RM. This will lead to resolving kernels $A^{(k)}$ that are hard to interpret despite the small uncertainty. Thus, a large target kernel size $T^{(k)}$ is needed to counteract this effect and we typically end-up having low resolution and low uncertainty. On the contrary, a large $T^{(k)}$ in a data-dense area will usually lead to a small RM with a small uncertainty. Therefore, the $T^{(k)}$ can be made smaller, allowing us to probe smaller scale structures, which then leads to an increase in the uncertainty (with a higher resolution). This is the reason for using the ray count as a proxy for designing the $T^{(k)}$ (*a priori* resolution). In our application of SE Asia, we choose these to be 3-D spheroids, to achieve the best resolution-uncertainty compromise. The target kernel size varies from the cells' circumscribed spheroids to 6 times this size laterally, proportional with the inverse of the ray count, to allow for smaller $T^{(k)}$ volumes. We add an upper limit for the ray count to handle cells with very large numbers of rays (with the limit larger for the P-wave inversion due to the presence of more data compared to S). The resulting lateral radii of the target kernels are shown in Fig. 2(c).

Thanks to SOLA (see eq. 1), we can control the $\mathrm{dln}V_p$ and $\mathrm{dln}V_s$ local resolutions ($A^{(k)}$) and aim for them to be as close as possible to each other. To achieve this, we use the same target kernel size for both at each enquiry point, taking the largest size based on the P- and S-phase ray counts. This approach is similar to that in Restelli *et al.* (2024), who also aimed to obtain similar P and S resolution kernels in SOLA inversions, but in a 1-D application of normal-mode data. Finally, the localized averaged velocity anomaly estimate is computed from the generalized-inverse coefficients and the data:

$$\hat{m}^{(k)} = \sum_{i=1}^{N} x_i^{(k)} d_i . \tag{4}$$

With SOLA, we only need to invert for chosen enquiry cells, within the region of study. This allows for the use of teleseismic data travelling outside the region as well. For this reason, our tomographic grid consists of two grids with different cell sizes: we have an inner grid [black rectangle in Fig. 1(a)], which covers more than the whole region of study, within [90◦, 136◦] longitude, [−18◦, 10◦] latitude and [0 km, 1000 km] depth, with fine cell sizes of $0.5\circ \times 0.5\circ \times 50$ km. This covers a larger area than the region of interest [yellow rectangle in Fig. 1(a)] to study potential smearing on the edge of the region. We use a coarser grid (outer grid) to cover the rest of the Earth's mantle, using coarser cells of $2\circ \times 2\circ \times 100$ km. A summary of the tomography setup is displayed in Fig.2

3.2 Metrics to assess the similarity of resolution for *P* and *S*

In addition to using identical P and S target kernels, we use three metrics to evaluate the similarity of the 3-D resolving kernels for the P- and S-wave inversions ($A_P^{(k)}$ and $A_S^{(k)}$, respectively), with the overall aim to achieve these at a comparable resolution: the misfit of the $A_P^{(k)}$ to the $A_S^{(k)}$ kernel (Rdiff), the peak signal to noise ratio (PSNR) and the Jaccard ratio metric.

- The 'Rdiff' metric (see eq. 5) is the misfit between $A_P^{(k)}$ and $A_S^{(k)}$ normalized by the volume of $A_S^{(k)}$:

$$\mathrm{Rdiff}^{(k)} = \frac{\int \left(A_P^{(k)} - A_S^{(k)}\right)^2}{\int \left(A_S^{(k)}\right)^2} = \frac{\sum_{j=1}^{M} V_j \left(A_{P,j}^{(k)} - A_{S,j}^{(k)}\right)^2}{\sum_{j=1}^{M} V_j \left(A_{S,j}^{(k)}\right)^2} . \tag{5}$$

For similar $A_P^{(k)}$ and $A_S^{(k)}$, the Rdiff value should be small, and ideally close to zero.

- The PSNR (see eq. 6) is generally used in the context of image compression to measure the similarity between two images. In our case, because $A^{(k)}$ contains many values close to zero, the PSNR effectively only provides information on how voluminous $A^{(k)}$ is. While the PSNR resembles the Rdiff value since both rely on misfits of the form $\left(A_{P,j}^{(k)} - A_{S,j}^{(k)}\right)^2$ (e.g. Nasrabadi *et al.* 2014), it is not normalized:

$$\mathrm{PSNR}^{(k)} = 20 \log_{10} \frac{2}{\sqrt{\underset{\text{all layers}}{\text{mean}} \left(\underset{j\in\text{one layer}}{\text{mean}} \left(V_j [A_{P,j}^{(k)} - A_{S,j}^{(k)}]^2 \right) \right)}} . \tag{6}$$

Unlike Rdiff, the PSNR is sensitive to the size of $A^{(k)}$ as $\int A^{(k)} = 1$. As a result, misfits tend to be larger for smaller kernels. With most cells zero, the few non-zero misfit values strongly influence the PSNR as we consider averages in eq. (6). For voluminous $A^{(k)}$, these misfits are small, leading to high PSNR values. Conversely, confined $A^{(k)}$ produce large misfits and lower PSNR values.

- The Jaccard metric (see eq. 7), commonly used in mathematics, states how two sets spread over the same volume, by dividing their intersection over their union. To define the volumes of $A_P^{(k)}$ and $A_S^{(k)}$ to be used in such a metric, we only consider cells with significant

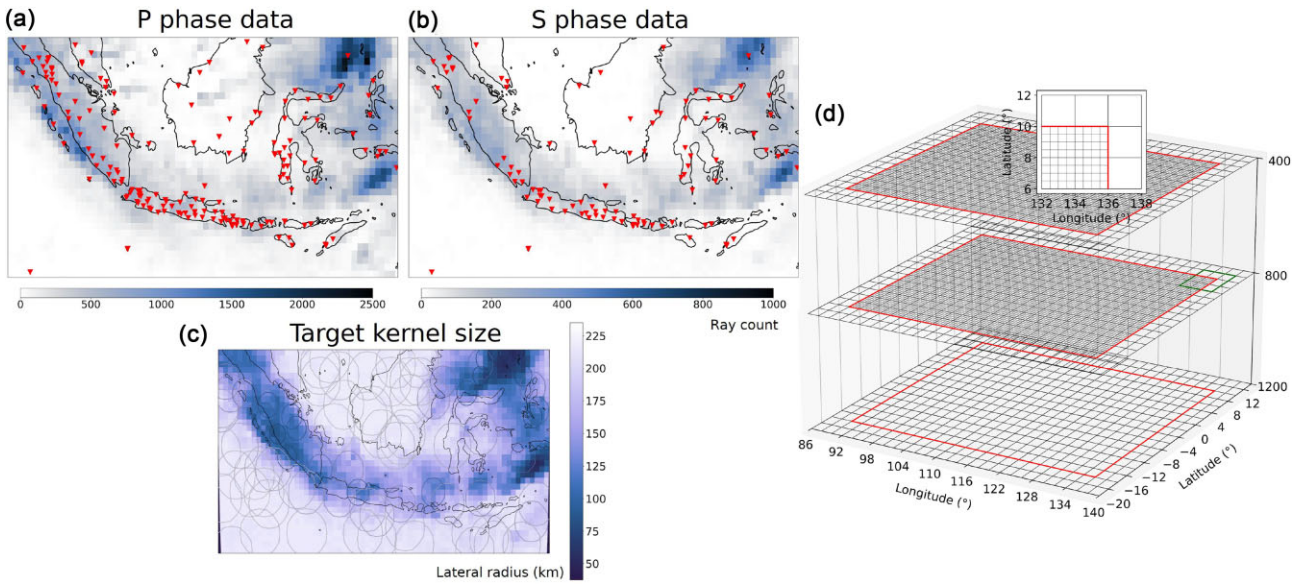

Figure 2. Summary of the tomography setup using SOLA. (a) and (b) show the *P* and *S* ray counts at 475 km depth, respectively, while (c) indicates the lateral radius of each $T^{(k)}$, computed from the inverse of the ray counts. The $T^{(k)}$ are adapted to have similar sizes, even though the *S*-wave subset is smaller. Examples of target kernels are shown in (c). Stations used in both *P* and *S* subsets are represented by inverted red triangles. (d) 3-D scheme of the tomography grid, with a fine mesh of $0.5\circ \times 0.5\circ \times 50$ km within the black rectangle of Fig. 1(a), down to 1000 km depth, and a coarser mesh of $2\circ \times 2\circ \times 100$ km covering the remaining mantle of the Earth.

amplitudes, that is, greater than 15 per cent of the maximum of either $A_P^{(k)}$ or $A_S^{(k)}$. This 15 per cent threshold was found by trial-and-error. This metric can be written as:

$$\text{Jaccard} = \frac{\text{Volume}\,(P \cap S)}{\text{Volume}\,(P \cup S)}\,, \tag{7}$$

where $P = \left\{\text{cells}\, j \mid A_{P,j}^{(k)} > 0.15 \max\left(A_P^{(k)}\right)\right\}$ and likewise for *S* with $A_S^{(k)}$. When the two sets $A_P^{(k)}$ and $A_S^{(k)}$ become more similar, the Jaccard value gets closer to one.

The combination of the three metrics offers a robust way to compare the $A^{(k)}$ for the *P*- and *S*-wave models. Particularly, it is useful to consider the Rdiff and PSNR jointly. For confined $A^{(k)}$, even small volumetric differences in $A_P^{(k)}$ and $A_S^{(k)}$ could yield large Rdiff values, but their overall impact is limited due to the size of the volume. In this case, less weight should be given to Rdiff. Voluminous $A^{(k)}$ tend to easily span different grid cells, so a small Rdiff is needed to achieve similarity. In other words, more weight should be given to Rdiff in that case. To ensure similar $A_P^{(k)}$ and $A_S^{(k)}$, we therefore define thresholds for a combination of the PSNR and Rdiff values as well as for the Jaccard metric. We consider $A_P^{(k)}$ and $A_S^{(k)}$ to be comparable when two thresholds are achieved:

$$\begin{aligned} &\text{Jaccard} > 0.45\,, \\ &\text{Rdiff} \quad \lesssim \quad -2.24\text{e}{-2} \times \text{PSNR} + 2.353\,. \end{aligned} \tag{8}$$

These threshold values are obtained after visual inspection of a subset of 600 cells, with the aim to eliminate more false negatives than false positives, and to be conservative on the final selection of comparable *P* and *S* resolving kernels. We illustrate the results of this visual inspection for the combined PSNR and Rdiff metric in Fig. 3(a), which confirms that the PSNR or Rdiff could not have been used individually, while we show the threshold for the Jaccard in Fig. 3(b). Strictly similar $A_P^{(k)}$ and $A_S^{(k)}$ should lead to a high PSNR value by definition, but the Rdiff will be tiny, such that this is not an issue for the threshold. We tried out circa 20 different metrics, but the PSNR–Rdiff combination seems to work best for this study, given that we have cells of rather similar volume across the region of interest. Yet, other metrics or combinations could be used, for example using the resolution misfit—eq. (3). In studies with different geometries, this could be normalized by the integral of the $T^{(k)}$ (e.g. Restelli *et al.* 2024).

To illustrate different metrics combinations, Fig. 3(c) shows slices of $A_P^{(k)}$ and $A_S^{(k)}$ for different cells (k). The Jaccard metric only relates to the volume of the resolution kernels that have significant values, without giving importance to the potential differences in amplitude. On the contrary, the two misfit metrics (PSNR and Rdiff) only reflect the amplitude differences in the resolving kernels. Consequently, we observe that when the Jaccard threshold is not reached, but the misfit one is (second column), the low amplitudes are generally spread over different volumes even if the maximum amplitudes are relatively similar. On the contrary, when the Jaccard criterion is satisfied, but the misfit one is not (third column), the amplitudes are rather different even if the volume of both resolution kernels is similar. When both criteria are met (first column), or not (last column), we observe the best or worse of all metrics: we either have similar amplitudes over similar volumes (comparable *P* and *S* resolution), or different amplitudes over different volumes (very different resolution), respectively. Thus, we use these metrics to compute a first mask, which serves to only display the *P* and *S*-wave models where their resolution is deemed to be comparable.

3.3 The Hinkley distribution

We aim to compute the ratio $R^{(k)} = \hat{m}_S^{(k)}/\hat{m}_P^{(k)}$ for all cells k with comparable resolving kernels $A_P^{(k)}$ and $A_S^{(k)}$. Since in the SOLA framework, $\hat{m}_S^{(k)}$ and $\hat{m}_P^{(k)}$ are local-average estimates with corresponding Gaussian uncertainties, $\sigma_{\hat{m}_S^{(k)}}$ and $\sigma_{\hat{m}_P^{(k)}}$, their division (i.e. $R^{(k)}$) results into the Hinkley distribution, H. This distribution is

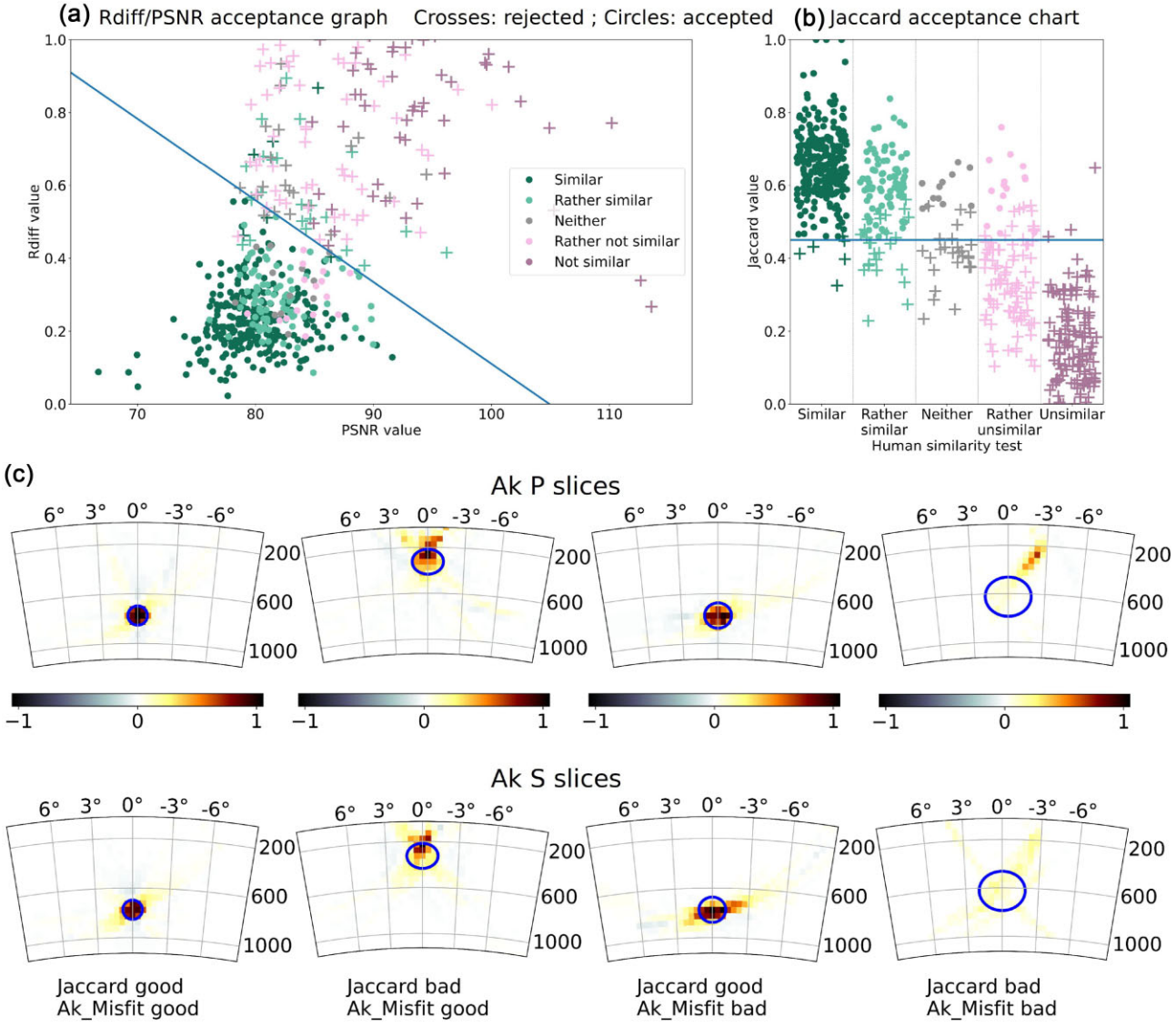

Figure 3. Illustration of the metrics used to assess the similarity of P and S resolution applied to a subset of random cells. (a) Combination of the PSNR and Rdiff metrics and (b) the Jaccard metric for the similarity assessment of the resolving kernels ($A^{(k)}$). A subset of 600 cells were visually inspected to define the similarity of $A_P^{(k)}$ and $A_S^{(k)}$. The straight blue lines represent the Rdiff $= -2.24\text{e}{-2} \times$ PSNR $+ 2.353$ (a) and the Jaccard $= 0.45$ (b) equations, respectively. A plus corresponds to a cell that is deemed to differ in terms of the P and S resolution, because of either the Jaccard or the PSNR/Rdiff metrics (the combination is named 'Ak_Misfit'). Cells having similar P and S resolution are represented by circles. (c) Slices of normalized resolving kernels $A_P^{(k)}$ (top) and $A_S^{(k)}$ (bottom) at four different locations k. These were chosen to illustrate several scenarios for the metrics, that is, a location (from left to right) where both conditions are respected; only one condition is respected (Ak_Misfit is, but Jaccard is not); only the other condition is respected (Jaccard); none of the conditions are respected.

computed analytically (Hinkley 1969):

$$H(w) \sim \frac{N_1(\mu_1,\, \sigma_1^2)}{N_2(\mu_2,\, \sigma_2^2)}(w), \tag{9}$$

where $\mu_{1,2}$ and $\sigma_{1,2}$ represent the mean and standard deviation of the two uncorrelated Gaussians (i.e. $\text{dln}V_s$ and $\text{dln}V_p$ in each cell). The complete analytic equation can be found in the Supplementary Materials section Ss1, eq. (Se1).

For further interpretation of the ratio R, we are only interested in cells where the Hinkley distribution resembles a Gaussian, as Gaussian uncertainties are easier to interpret. To assess when the Hinkley distribution is close to a Gaussian, we compute the following misfit:

$$\text{Misfit} = \int_{w\in[-15,15]} \frac{(H(w) - \text{BGF}(w))^2}{H(w)^2}\text{d}w\,, \tag{10}$$

with BGF the Gaussian function (Best-fitting Gaussian Function) that best fits the Hinkley distribution (H). We do not consider w with absolute values larger than 15, as these likely result from a division with a denominator close to zero. The BGF is found using a Nelder-Mead simplex algorithm (Nelder & Mead 1965), by determining the mean μ and variance σ^2 of a normal distribution N that minimize the L_2 norm of the function $f(w) = H(w) - N(w, \mu, \sigma^2)$. We consider Hinkley to be Gaussian-like when the misfit (see eq. 10) is smaller than 10 per cent. In that case, the values of μ and σ represent our estimates of the ratio $R = \text{dln}V_s/\text{dln}V_p$ and its uncertainty, respectively. We illustrate the determination of the ratio R using Hinkley in Fig. 4, where we show examples for cells k with a misfit above and below the 10 per cent limit. Based on this misfit, we set up a second mask, with the aim to only interpret

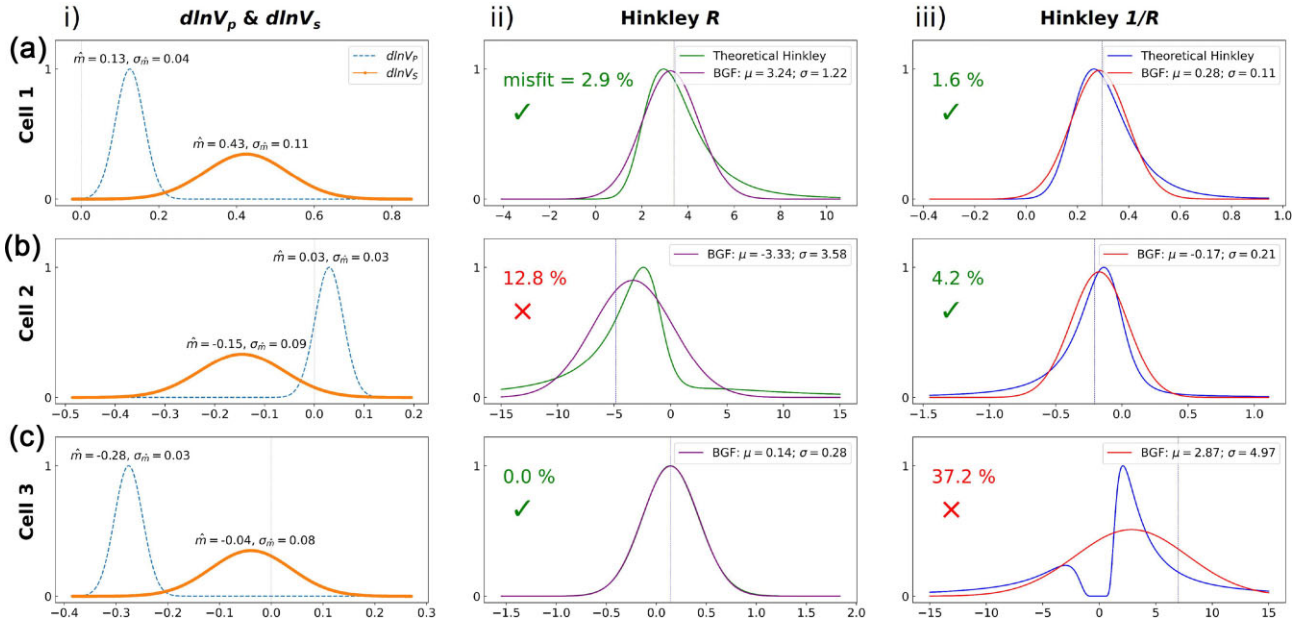

Figure 4. Examples of the Hinkley distributions for three different cells (a,b,c). For each example, we show: (i) the $\mathrm{dln}V_p$ (dotted blue) and $\mathrm{dln}V_s$ (orange) SOLA distributions; (ii) the $\mathrm{dln}V_s/\mathrm{dln}V_p$ Hinkley distribution (green) and its best-fitting Gaussian function (BGF, here in purple) and (iii) the $\mathrm{dln}V_p/\mathrm{dln}V_s$ Hinkley distribution (blue) with its BGF (red). In the top example, both ratios are considered Gaussian; in the middle, only $\mathrm{dln}V_p/\mathrm{dln}V_s$ and in the bottom example, only $\mathrm{dln}V_s/\mathrm{dln}V_p$ is Gaussian. In panels of R and $1/R$, we also indicate the misfit between the Hinkley distribution and the BGF defined in eq. (10).

cells k for which the division of $\hat{m}_S^{(k)}$ with $\hat{m}_P^{(k)}$ results in a Gaussian-like distribution of $R^{(k)}$. The same approach is also applied to the $\mathrm{dln}V_p/\mathrm{dln}V_s$ ratio ($1/R$).

4 RESULTS AND DISCUSSION

We present hereafter the SPRUM-Indo model, which describes $\mathrm{dln}V_s$, $\mathrm{dln}V_p$ and their ratio (R) beneath Indonesia along with the uncertainties using SOLA with body wave data in ray theory. To ensure a meaningful joined interpretation of $\mathrm{dln}V_s$ and $\mathrm{dln}V_p$ and their ratio R [see Fig. 5(a) for 475 km depth and Fig. S2– S5 for other depths], we first combine the two masks discussed in the Methods to create a final mask [Fig. 5(c) and Fig. S1]. This allows us to infer maps of $R = \left(\mathrm{dln}V_s/\mathrm{dln}V_p\right)$ and $1/R = \left(\mathrm{dln}V_p/\mathrm{dln}V_s\right)$, with their associated uncertainties on the remaining cells, using the Hinkley distribution [Fig. 5(d)–(e) for 475 km depth and Fig. S6– S9 for additional depths].

4.1 Resolution and Hinkley masks

While the resolution mask (Fig. 5c) is correlated with the data coverage distribution (Fig. 2), the Hinkley mask is linked to the ratio between the anomaly values in the denominator (either $\mathrm{dln}V_p$ or $\mathrm{dln}V_s$ for R or $1/R$, respectively) and their uncertainties, $\sigma_{\hat{m}^{(k)}}/\hat{m}^{(k)}$ (Fig. 4). When this ratio is high—meaning the amplitude of the uncertainty is comparable to the amplitude of the anomaly itself—the Gaussian distribution of the denominator may cross zero. In that case, the division is likely to become unstable, leading to a loss of normality in the R (or $1/R$) ratio and a failure of the Hinkley test. However, we typically find that our inversion results in relatively low uncertainties for both $\mathrm{dln}V_p$ and $\mathrm{dln}V_s$. As a result, the resolution mask is typically the most restrictive.

For the division method, when uncertainties are not available, the preferred approach is to discard grid cells where one of the parameters is close to zero, since Hinkley fails when the Gaussian distribution of the denominator crosses zero (as done, for instance, by Della Mora *et al.* 2011; Koelemeijer *et al.* 2015; Tesoniero *et al.* 2016; Lu *et al.* 2019). However, our analysis of the R ratio using Hinkley shows that it is sufficient to discard only $\mathrm{dln}V_p$ values close to zero, increasing the number of potentially computable ratios. Moreover, the use of more independent data reduces the final uncertainties. Therefore, inverting all available P-wave data, as is possible with the SOLA method, is more beneficial than reducing the data set to match the number of S-wave data. In fact, the ratio of model uncertainty over model amplitude ($\sigma_{\hat{m}^{(k)}}/\hat{m}^{(k)}$) is typically lower for $\mathrm{dln}V_p$, making the inference of $\mathrm{dln}V_s/\mathrm{dln}V_p$—the R ratio popularized by Masters *et al.* (2000)—more reliable than $\mathrm{dln}V_p/\mathrm{dln}V_s$, thus resulting in fewer masked cells (Fig. 5c). Unfortunately, computing Hinkley using absolute velocity values that are never zero to bypass these issues is not feasible. Supplementary Materials section Ss2 demonstrates that this approach leads to a nonlinear problem that cannot be easily solved, as it involves local averages over multiple depths that have different reference model values.

When Hinkley does not follow a perfect Gaussian distribution, the value of its ratio R differs from the ratio obtained by directly dividing $\mathrm{dln}V_s$ by $\mathrm{dln}V_p$. However, when Hinkley is Gaussian, both ratios are equal. This may explain artefacts observed in other studies when dividing $\mathrm{dln}V_s$ and $\mathrm{dln}V_p$ in regions with seemingly similar resolution (e.g. Fang *et al.* 2018; Zenonos *et al.* 2020). Setting aside the fact that their resolution assessment is purely based on resolution tests, these studies also did not include uncertainties on the velocity distributions. As a result, the division may be unreliable, leading to differences in the computed R values (with and without Hinkley). Moreover, when only one of R or $1/R$ can be obtained using Hinkley, it is not possible to obtain the other ratio by simply taking the inverse of the ratio that works. Indeed, if we assume the R Hinkley distribution is non-Gaussian, while $1/R$ is Gaussian, we can reproduce the expected

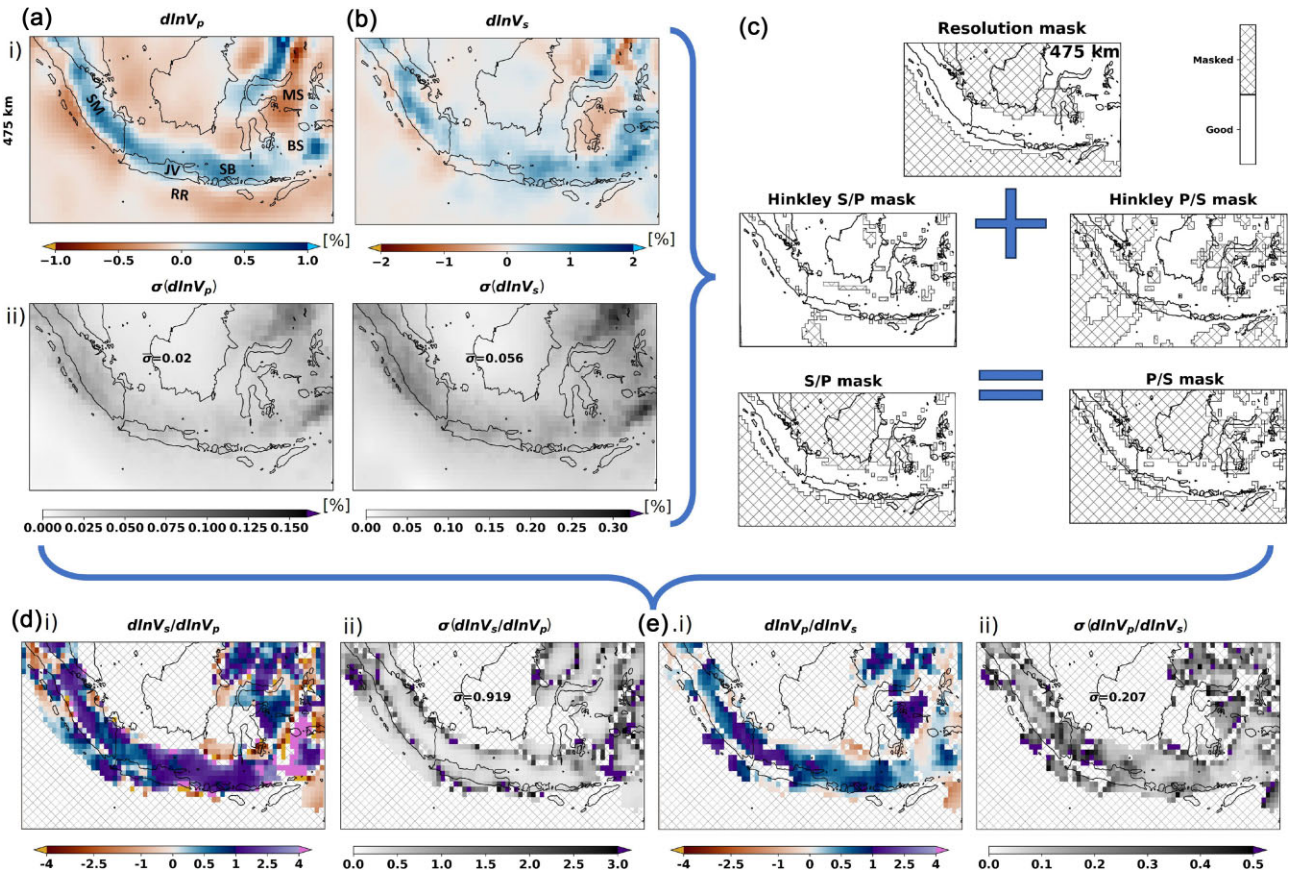

Figure 5. Results of the SOLA inversion at 475 km depth for $\mathrm{dln}V_p$, $\mathrm{dln}V_s$, $\mathrm{dln}V_s/\mathrm{dln}V_p$ and $\mathrm{dln}V_p/\mathrm{dln}V_s$, shown in (a), (b), (d) and (e), respectively, including their uncertainties. The standard deviation indicated in the uncertainty maps represents the mean uncertainty of all cells present in a given map. (c) The $\mathrm{dln}V_p$ and $\mathrm{dln}V_s$ maps are used to compute the resolution and Hinkley masks, showing where $\mathrm{dln}V_p$ and $\mathrm{dln}V_s$ have similar local resolution and where their ratios are interpretable. The combination of both indicates where the ratios can be interpreted. SM: Sumatra, JV: Java, RR: Roo Rise, SB: Sumbawa, BS: Banda Sea, MS: Molucca Sea.

non-Gaussian Hinkley pdf of R by randomly drawing samples from the Gaussian Hinkley distribution of $1/R$ and creating a histogram of their inverses. Therefore, both R and $1/R$ must be computed using Hinkley, and we should only interpret the distribution that is Gaussian.

We define $R' = \frac{1}{1/R}$, as the inverse of the Hinkley value for $1/R$, which should be equal to the R value. When both ratios (R and $1/R$) are Gaussian, we observe a correlation between $|R - R'|$ and the misfit between the Hinkley distribution of R and its BGF (eq. 10). However, no correlation is found between $|R - R'|$ and the misfit of the $1/R$ Hinkley distribution and its BGF. This further confirms that when only R is non-Gaussian, the Gaussian distribution of $1/R$ (through R') cannot be used to compute R –in other words, $R \neq R'$. It is therefore crucial to obtain a reliable PDF using Hinkley and to determine precisely when it follows a Gaussian distribution, in order to obtain reliable R (or $1/R$) values and their uncertainties for meaningful interpretations. To summarize, the two ratios are only interchangeable when both follow a Gaussian distribution. Indeed, for all cells where both ratios follow a Gaussian distribution, the median of $\{|R - R'|\}$ is about 0.17 times the median of the uncertainties in R ratio—i.e. the uncertainty in R is much larger than the difference between R and R', but only if both ratios are Gaussian.

4.2 Sensitivity of Hinkley to data uncertainties

Estimating data uncertainties is a complex task that directly affects model uncertainties and, consequently, the computation of the ratio using Hinkley. Here, we investigate the sensitivity of the ratio to the data uncertainties by simulating their perturbation while keeping the velocity values fixed. We then compute many Hinkley distributions with different uncertainty combinations and assess whether they are Gaussians. We use the proportion of Gaussian-like distributions we obtain in this process as a way to quantify the sensitivity and the potential errors in the data uncertainty estimation that may be due to the crustal model or errors in source parameters.

To determine the extent of data uncertainty perturbations, we define an amplification factor α_i for each data based on its seismic phase: 1.2 for the direct P and S phase and 1.5 for the pP and sS phase, meaning that $\sigma_{i,P}$ or $\sigma_{i,sS}$ could be up to 1.2 or 1.5 times larger. This is similar to the upscaling factor of Latallerie *et al.* (2025) for instance. We then compute the quadratic average α of these factors for the entire P and S data sets as follows:

$$\alpha = \sqrt{\frac{\sum_i^N \alpha_i^2}{N}}\,, \tag{11}$$

where i is the data index and N the number of data. Using this quadratic average, 1.24 for P and 1.23 for S phase, we define a new,

larger model uncertainty for the k-th cell $\sigma'_{\hat{m}(k)}$:

$$\sigma'_{\hat{m}(k)} = \alpha \times \sigma_{\hat{m}(k)}. \tag{12}$$

Assuming that the difference between this new model uncertainty and the estimated SOLA model uncertainty represents the error in the uncertainty estimation, we have:

$$\sigma'_{\hat{m}(k)} - \sigma_{\hat{m}(k)} = \sigma_{\hat{m}(k)} \times (\alpha - 1)\,. \tag{13}$$

Thus, Hinkley's sensitivity of data uncertainties is the proportion of Gaussian-like Hinkley distributions within the ranges of uncertainty $\sigma_{\hat{m}(k)} \pm \sigma_{\hat{m}(k)} \times (\alpha - 1)$ [shown by the red rectangles in Figs 6(a) and (c) for two cells], because the true model uncertainties $\sigma'_{\hat{m}(k)}$ (for P and S) are expected to fall in those ranges. At the example depth of 475 km (Fig. 6b), we observe that the proportion of Gaussian-like Hinkley distributions is close to 100 per cent for R, except near the edges of the unmasked area, while for $1/R$, we find large areas where the Hinkley distribution is Gaussian-like only 20 per cent of the time. This further suggests that the determination of the R ratio is more stable than the determination of $1/R$. Interesting patterns are observed when we examine slices of the Hinkley–BGF threshold maps, where we mask areas where the misfit is above 10 per cent (Figs 6a and c). Most of what we observe is expected; Hinkley becomes non-Gaussian as the $\mathrm{dln}V_p$ (panels ii) or the $\mathrm{dln}V_s$ (panels i) distribution crosses zero. However, sometimes the distribution crosses zero and yet still results in a Gaussian ratio. This further highlights the instability of Hinkley and underscores the fact that confidence in the model uncertainties is very important for reliable inferences of the ratio. As the sensitivity approaches 100 per cent, Hinkley is stable and robust to variations in data uncertainty. However, if the sensitivity is close to zero, accurate data uncertainty estimation is crucial to trust the computed ratio. Based on this sensitivity analysis, it would be possible to define a third mask to exclude regions with Hinkley ratios that are less stable. However, as we would need to choose a threshold, we did not apply such a mask in this study to avoid introducing another subjective choice.

4.3 Structural interpretation of SPRUM-Indo

The complexity of the SE Asia region is clearly visible in our results, for instance in the $\mathrm{dln}V_p$ and $\mathrm{dln}V_s$ models [see Figs 5(a) and (b) for 475 km depth and Figs S2, S4 for other depths]. While we present our results as depth slices, we want to stress that the structure at each location represents a local average over a larger region (defined by the resolution). To interpret the velocity anomalies, we thus always need to consider also the model uncertainty and resolving kernel (see Figs S3, S5 for $\mathrm{dln}V_p$ and $\mathrm{dln}V_s$ uncertainties respectively, for other depths).

Multiple subducting slabs stand out, such as the Java-Sumatra slabs, the spoon-shaped slab in the Banda region and the two slabs with opposing subduction in the Molucca Sea. At shallow depths, the slabs appear relatively thin, widening from the mantle transition zone (MTZ) down to the lower boundary of our model (800 km depth). The continuity of the slabs is also clearly visible. In addition, well-defined low-velocity regions are observed, such as the one between the Molucca Sea slabs and another beneath the Sumatra slab. While a detailed interpretation of the region is beyond the framework of this study, we will briefly discuss below two distinctive features: the Java slab hole and the Sumatra subslab hot mantle upwelling (SHMU).

4.3.1 The Java slab hole

The Java slab hole was first discussed by Widiyantoro *et al.* (2011) and Hall & Spakman (2015). Widiyantoro *et al.* (2011) did not specify its size, but their models suggest it is similar to the description of Hall & Spakman (2015): a 250–500 km deep, 400–500 km wide reduction in the fast velocity anomaly between 109 and 115○E (indicated by the target kernel in Fig. 7).

Hall & Spakman (2015) proposed that a buoyant structure in the slab caused subduction to pause about 8 Myr ago, supported by high-K alkalic backarc volcanism of the same age. While Zenonos *et al.* (2019) and Toyokuni *et al.* (2022) agree with this origin, their models show smaller sizes for the slab hole: 350–500 km (Zenonos *et al.* 2019) or 280–430 km (Toyokuni *et al.* 2022). Toyokuni *et al.* (2022) also found that the subslab mantle and mantle wedge materials could be connected between 310 and 400 km depth. Further studies by Wang *et al.* (2022) and Xie *et al.* (2023) agree on the size, but they suggest that the velocity estimates are uncertain due to a lack of data. They could therefore also be interpreted as a thinning of the slab, instead of a hole (Wang *et al.* 2022). A second hole beneath East Sumbawa has also been suggested by some studies (e.g. Widiyantoro *et al.* 2011; Hall & Spakman 2015; Zenonos *et al.* 2019; Wehner *et al.* 2022). Yet, none of these studies analysed their tomographic model uncertainty or resolution. While they did perform sensitivity tests, these do not provide reliable information on the true model resolution.

In our model [Fig. 7, where the supposed Java and Sumbawa holes are respectively indicated with 'JV' and 'SB' in the $\mathrm{dln}V_p$ slice (b)], we observe a slight reduction in the P-wave velocity amplitudes, consistent with the results of Zenonos *et al.* (2020) [see the models for Central Java in Fig. S10(b)], though Toyokuni *et al.* (2022) (Fig. S10c) shows a stronger positive anomaly and slab deflection northward. At the locations of both suggested holes, $\mathrm{dln}V_s/\mathrm{dln}V_p$ anomalies (Fig. 8 and Figs S6–S9 for other depths) largely exceed values of 2.5, with uncertainties around 1. This is again rather consistent with Zenonos *et al.* (2020) (Fig. S12), but in their model the anomaly is less pronounced at the location of the main hole. While these regions have slightly higher ratio uncertainties compared to their surroundings, they show no significant changes in their $\mathrm{dln}V_p$ and $\mathrm{dln}V_s$ uncertainties.

Seismicity data indicate no earthquakes at the location of the supposed holes (Fig. 7b). However, we observe no overall correlation between seismicity and the R values of the SOLA model. Since 250–500 km is the least seismogenic depth range (e.g. Tsampas *et al.* 2017), this may not be relevant. Furthermore, the $A^{(k)}$ is well contained within the area with reduced P-wave velocity amplitudes (Fig. 7b), indicating a good resolution. At the same time, the amplitude reduction is significant given the model uncertainty, indicating reliable results. However, the main hole is absent in the S-wave model, similar as in the results of Zenonos *et al.* (2019) and Wehner *et al.* (2022) [see Fig. S11(b) and (c) for their respective S-wave models]. We note a slight amplitude reduction in our S-wave model near the location of the second hole near Sumbawa between 300 and 400 km depth, even though it is 100 km deeper than seen in the models of Widiyantoro *et al.* (2011) and Wehner *et al.* (2022). If the proposed slab holes exist, they must therefore be smaller than the resolution of our model. Alternatively, the subduction of structures like the Roo Rise could affect the thermochemical properties of the slab, serving as alternative explanation of the reduced $\mathrm{dln}V_p$ amplitudes, unaffected $\mathrm{dln}V_s$ amplitudes and the lack of seismicity.

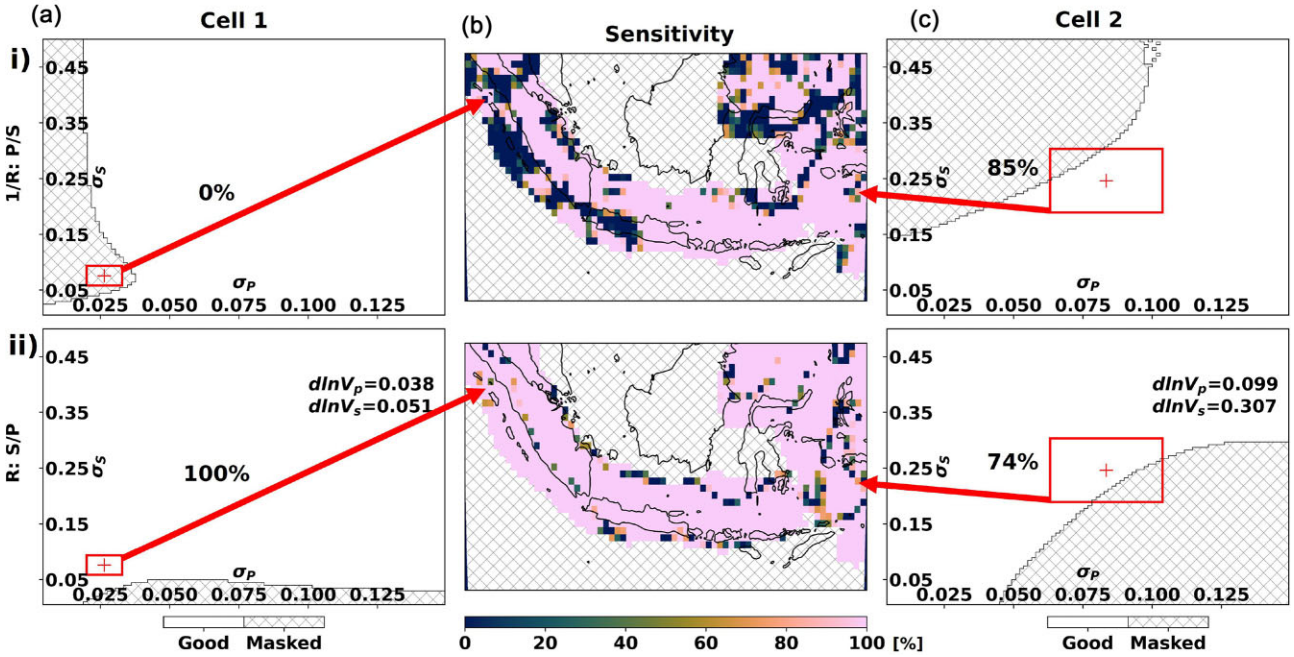

Figure 6. Sensitivity of the ratio computation to data uncertainty perturbations, shown for two example cells (a and c), for both $\frac{\mathrm{dln}V_p}{\mathrm{dln}V_s}$ and $\frac{\mathrm{dln}V_s}{\mathrm{dln}V_p}$ estimation (i and ii). The non-hatched and hatched cells correspond to those combinations of uncertainties for which the misfit between Hinkley and its BGF is below or above 10 per cent, respectively, that is, whether the Hinkley can be considered Gaussian or not. (b) Maps of the sensitivity computed for all cells in the 475 km depth layer. For each cell, we express the proportion of Gaussian-like Hinkley distributions that are obtained for the possible velocity–uncertainty combinations we consider. The velocity values are fixed, and the uncertainties are linearly chosen in the range $(1 \pm 0.24) \times \sigma$ for the P phases and $(1 \pm 0.23) \times \sigma$ for the S phases (where the value is determined by the relative number of direct and depth phases).

4.3.2 The Sumatra subslab hot mantle upwelling (SHMU)

Underneath the Java-Sumatra slab at 200 km depth, a strong and large negative velocity anomaly is present. This so-called subslab hot mantle upwelling (SHMU) might have different causes: it could be due to a return flow rising along the slab as it is subducting in the lower mantle (e.g. Toyokuni *et al.* 2022) or could represent flow due to the retreat of the Indo-Australian plate (e.g. Long & Silver 2008; Fan & Zhao 2021). It has been suggested that these low-velocity anomalies may trigger megathrust earthquakes, because their buoyancy increases the normal and/or shear stress in nearby areas (e.g. Fan & Zhao 2021; Toyokuni *et al.* 2022). Additionally, Nugraha *et al.* (2019) found a link between earthquake production zones and unusual V_p/V_s values.

In our models (see Fig. 9 for slices at 475 km depth and Figs S2–S5 for other depths), the SHMU structure appears in both *P*- and *S*-wave models, a feature that is also seen in the *S* model of Zenonos *et al.* (2019), but absent in the *S* model of SASSY21 (Wehner *et al.* 2022) and the *P* model of Zenonos *et al.* (2019). It is well resolved as the resolving kernels are clearly focused with a lateral extent smaller than the SHMU itself. In addition, the uncertainties are lower than the velocity amplitudes, though they are slightly higher than in nearby areas. In both *P*- and *S*-wave models, the negative anomalies seem to arise from deeper than the model's lower boundary. However, in the *P*-wave model the low-velocity anomaly is only observed up to 175 km depth, while in the *S*-wave model, it continues to the surface. This discrepancy could arise from differences in the crustal corrections that are applied to *P* and *S* rays, particularly if V_p and V_s are not equally well constrained in the crustal models.

The $\mathrm{dln}V_s/\mathrm{dln}V_p$ anomaly varies with depth (see Fig. 10 for slices at 475 km depth and Figs S6–S9 for other depths). At 275 km depth, R is strongly positive (around 3–4), but at 475 km, it is closer to 1. The uncertainties at these depths are relatively high (1 at 275 km and 0.3 at 475 km) albeit still lower than the model values, while at greater depth the ratio cannot be interpreted due to being masked. Near the surface, the SHMU shows large variations in $\mathrm{dln}V_s/\mathrm{dln}V_p$, with very negative values due to positive $\mathrm{dln}V_p$ and negative $\mathrm{dln}V_s$ values. These unusual R values may lead to more megathrust earthquakes (Nugraha *et al.* 2019), which seem to occur more frequently in the Sumatra slab than the Java slab. This remains a hypothesis, as the difference in megathrust frequency could also be due to the fact that the Sumatra megathrust fault is longer (e.g. Hutchings & Mooney 2021). Perhaps coincidentally, the SHMU is only visible below Sumatra in our models. This may be because upwelling mantle material passes through the hole under Java, enters the mantle wedge, thus encouraging local volcanism (e.g. Hall & Spakman 2015; Toyokuni *et al.* 2022) and weakening the SHMU in the upper mantle under Java (e.g. Fan & Zhao 2021). Alternatively, if no slab holes are present, geothermal processes due to the subduction of the Roo Rise could disrupt the mantle upwelling. An aborted ridge is also being subducted in northern Sumatra, leading to a difference in lithospheric structure beneath Sumatra and Java. It is younger and thinner under Sumatra (e.g. Conrad & Lithgow-Bertelloni 2006; Müller *et al.* 2008), which may also partly explain why the SHMU is located only beneath Sumatra.

Our model results appear consistent with the different volcanic rocks observed in Indonesia, with typically more felsic lavas found in Sumatra, while Java has more mafic lavas (see for instance Fig. 7b) (e.g. Romero *et al.* 2021). The subducting slab under Sumatra may

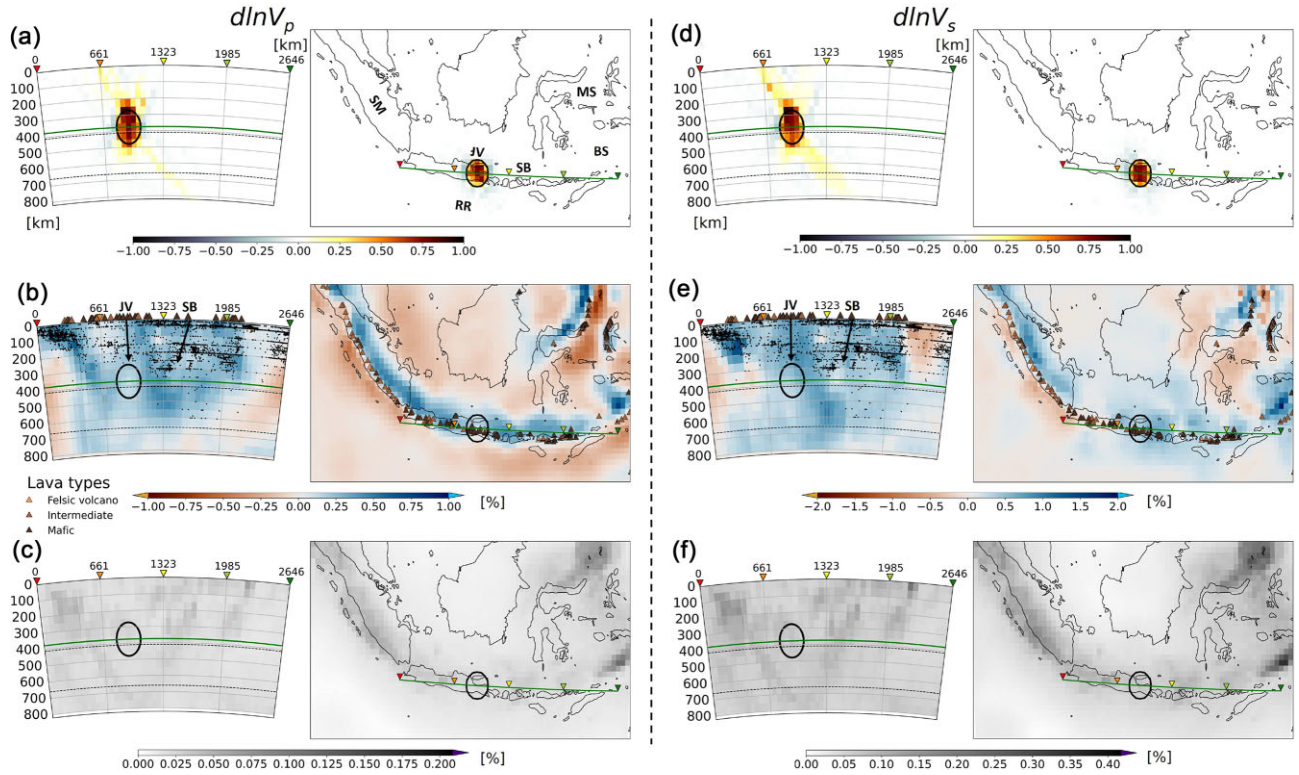

Figure 7. The region of the potential Java slab hole in the $\mathrm{dln}V_p$ model (b) with its uncertainties (c), represented by vertical (along the green line) and horizontal (at 375 km depth) slices. Seismic events reported by the ISC and volcanoes (Neumann van Padang & Association 1951) are represented by black dots and coloured upward triangles in (b,e), respectively. We only show here the events from the ISC-EHB (International Seismological Centre 2023b) and ISC-Reviewed (International Seismological Centre 2023a) data sets. The averaging kernel is also shown at the proposed location of the main slab hole (a), with the spatial extent of the target kernel indicated on all maps. The panels on the right similarly represent the $\mathrm{dln}V_s$ model (respectively e, f and d). Abbreviations are the same as indicated in Fig.5 In the (b) vertical slice, 'JV' and 'SB' are situated above the locations of the suggested main and Sumbawa holes.

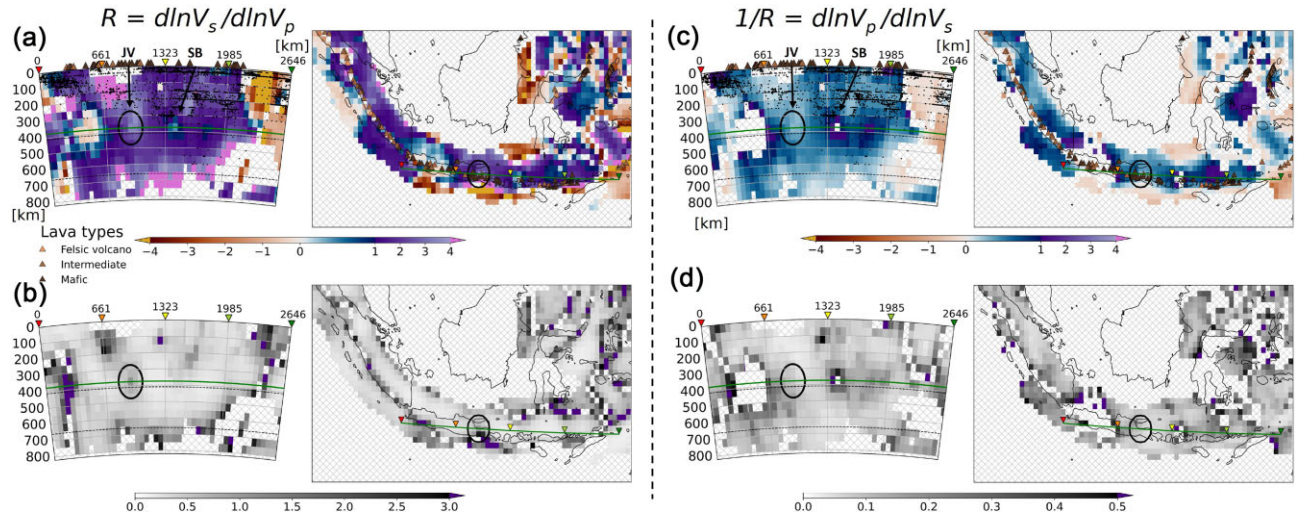

Figure 8. Same as Figs 7(b)–(f), but showing the $\mathrm{dln}V_s/\mathrm{dln}V_p$ (a, b) and $\mathrm{dln}V_p/\mathrm{dln}V_s$ (c, d) ratios.

thus be releasing more silica compared to Java, enriching the surrounding mantle and giving rise to felsic lava in the forearc volcanism. Since the SHMU appears spatially linked to the slab over a long distance, it may also be enriched with silica. This could explain the large negative anomaly of the SHMU and the differences between $\mathrm{dln}V_p$ and $\mathrm{dln}V_s$ at shallower depths, as silica would increase V_p more than V_s (e.g. Matsushima 1981). Above 200 km, slab dehydration might favour partial melting of the SHMU due to adiabatic decompression, reducing V_s more than V_p. This would reverse the sign between $\mathrm{dln}V_p$ and $\mathrm{dln}V_s$. Finally, the enrichment in light silicates could explain the high $\mathrm{dln}V_s/\mathrm{dln}V_p$ ratios as well as the buoyancy of the SHMU. This enrichment might increase gradually with greater depths, supported by the decrease in the ratio R from 200 to 700 km depth (Fig. 10a).

We note that it is complicated to perform a thorough interpretation of our results because of the nature of $\mathrm{dln}V_s/\mathrm{dln}V_p$ and the fact this

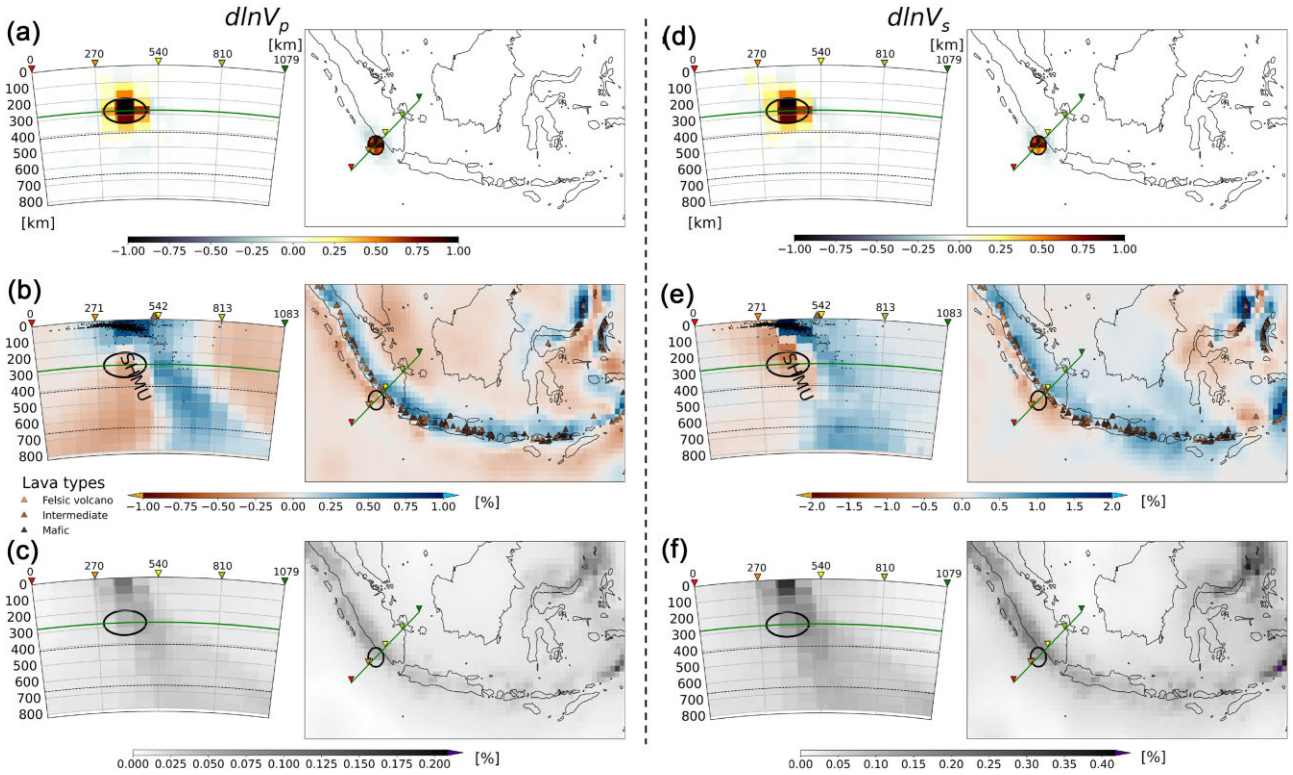

Figure 9. The region of the subslab negative velocity anomaly (SHMU), shown for both the $\mathrm{dln}V_p$ model (b, c) and the $\mathrm{dln}V_s$ model (e, f). An averaging kernel for the location of the SHMU is also shown (a, d), with the spatial extent of the target kernel indicated on all maps. For more details, see the caption of Fig.7

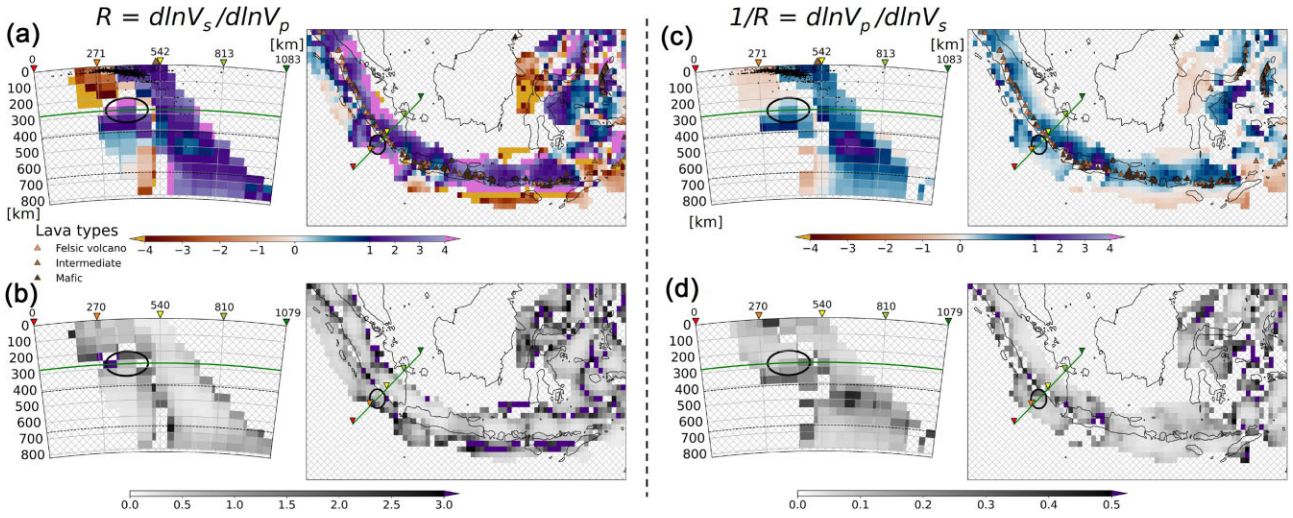

Figure 10. Same as Figs 9(b)–(f) for the $\mathrm{dln}V_s/\mathrm{dln}V_p$ (a, b) and $\mathrm{dln}V_p/\mathrm{dln}V_s$ (c, d) ratios.

is quite different from $\mathrm{dln}\left(V_p/V_s\right)$. The latter is well studied by other fields, especially in rock mechanics. Interpreting $\mathrm{dln}V_s/\mathrm{dln}V_p$ in terms of $\mathrm{dln}\left(V_p/V_s\right)$ helps to better understand the physical processes responsible for the observed seismic velocity variations. To this end, we have explored a new approach for interpreting models of $\mathrm{dln}V_s$, $\mathrm{dln}V_p$, R, $1/R$ and their uncertainties. As this is beyond the scope of this work, we will introduce this in a future study.

5 CONCLUSION

In this paper, we propose an approach to obtain estimates of the ratio R ($\mathrm{dln}V_s/\mathrm{dln}V_p$) and its uncertainties, which enable quantitative interpretations of Earth's interior structure. Using the SOLA-Backus-Gilbert method, we are able to construct models of relative velocity anomalies ($\mathrm{dln}V_p$ and $\mathrm{dln}V_s$) and their ratios ($\mathrm{dln}V_p/\mathrm{dln}V_s$ ($1/R$) and $\mathrm{dln}V_s/\mathrm{dln}V_p$ (R)), along with their uncertainties. We assess the similarity of the P and S-wave model resolutions using three metrics (Jaccard, PSNR and Rdiff) and use these to mask out regions where

the local model resolution is dissimilar. This approach allows us to use all data and to obtain individual models with better resolution and smaller uncertainties that propagate into the estimates of the ratio. Our approach using SOLA also enables us to include teleseismic data in regional models as the inversion is performed on a point-by-point basis.

We compute the velocity ratio using the Hinkley distribution, which accounts for the Gaussian uncertainties in $\mathrm{d}\ln V_p$ and $\mathrm{d}\ln V_s$. For easier geophysical interpretations, we assess whether the Hinkley distribution of R (and $1/R$) are Gaussian, and mask regions of the models where this is not the case. When the Hinkley distribution of R (or $1/R$) deviates too much from a Gaussian, the distribution of the inverse ratio is typically Gaussian-like. Therefore, it is essential to analyse which ratio is Gaussian after computing both Hinkley distributions, before making model interpretations.

We apply our methodology to study the mantle down to 800 km depth beneath Indonesia using a combination of the ISC-EHB and ISC-Reviewed data sets. Specifically, we develop models of $\mathrm{d}\ln V_p$, $\mathrm{d}\ln V_s$ as well as R and $1/R$ with resolution and uncertainty information. We find that the region of similar resolution for $\mathrm{d}\ln V_p$ and $\mathrm{d}\ln V_s$ roughly follows the region with good data coverage, emphasizing the need to use all possible data. Our models enable us to quantitatively confirm the presence of a subslab hot mantle upwelling beneath the Sumatra slab, but we found no conclusive evidence of slab holes under Java or East Sumbawa given the model resolution. From this application of our methodology to SE Asia, we note that the similarity in resolution is the most limiting factor for computing the ratio. It may therefore be possible to develop an algorithm to optimize the resolution-uncertainty trade-off by adjusting the target kernel size to increase the number of cells with similar resolution. Finally, with the four developed models for $\mathrm{d}\ln V_p$, $\mathrm{d}\ln V_s$, R and $1/R$, it is possible to interpret the structures in terms of the true V_p/V_s ratio. We propose an approach for this in a future study.

ACKNOWLEDGMENTS

We thank the Editor (Huajian Yao), Christine Houser and an anonymous reviewer for their constructive comments that have improved the manuscript. The authors would like to acknowledge the International Seismological Centre for their publicly available data sets, as well as their quick response to questions concerning the data set and their software. We are thankful to the High Performance Computing Center of the University of Strasbourg for supporting this work by providing scientific support and access to computing resources. PK gratefully acknowledges funding from the Royal Society through a University Research Fellowship (URF\R1\180377). For the purpose of open access, the authors have applied a CC BY public copyright license to any Author Accepted Manuscript version arising.

SUPPORTING INFORMATION

Supplementary data are available at *GJIRAS* online.

FINAL_SOM_Serra_etAl_GJI

DATA AVAILABILITY

The *discrete* SOLA tomography code consists in running the LSQR code with specific, *study-dependent*, input matrices and vectors, corresponding to personal choices (e.g. data kernels, model discretization, target kernels), as detailed in appendix A of Zaroli (2016). LSQR is available at (Stanford's Systems Optimization Laboratory): https://web.stanford.edu/group/SOL/software/lsqr/. Seismic events and code (ISCLOC) from the International Seismological Centre (ISC) are available at: http://www.isc.ac.uk/index.php. The code raydyntrace is available at: https://www.geoazur.fr/GLOBALSEIS/Soft.html. We use TauP (Crotwell *et al.* 1999) for ray tracing, as implemented in ObsPy (Beyreuther *et al.* 2010). All the tomographic results produced in this study are available at: https://doi.org/10.5281/zenodo.15480510.

REFERENCES

Aki, K., Christoffersson, A. & Husebye, E.S., 1977. Determination of the three-dimensional seismic structure of the lithosphere, *J. geophys. Res. (1896-1977),* **82**(2), 277–296.

Amiri, S., Maggi, A., Tatar, M., Zigone, D. & Zaroli, C., 2023. Rayleigh wave group velocities in north-west Iran: SOLA Backus-Gilbert vs. fast marching tomographic methods, *Seismica,* **2**(2).

Aryanti, E., Nugraha, A.D., Basuki, A. & Triastuty, H., 2018. *AIP Conf. Ser. Vol. 1987, 3D seismic tomography Vp, Vs and Vp/Vs ratio beneath Gede Volcano, West Java, Indonesia,* pp. 020046, Am. Inst. Phys.

Audet, P. & Bürgmann, R., 2014. Possible control of subduction zone slow-earthquake periodicity by silica enrichment, *Nature,* **510**(7505), 389–392.

Beyreuther, M., Barsch, R., Krischer, L., Megies, T., Behr, Y. & Wassermann, J., 2010. Obspy: a python toolbox for seismology, *Seismol. Res. Lett.,* **81**(3), 530–533.

Bolton, H. & Masters, G., 2001. Travel times of *P* and *S* from the global digital seismic networks: implications for the relative variation of *P* and *S* velocity in the mantle, *J. geophys. Res.: Solid Earth,* **106**(B7), 13 527–13 540.

Bondár, I. & Storchak, D., 2011. Improved location procedures at the international seismological centre, *Geophys. J. Int.,* **186**(3), 1220–1244.

Calò, M. & Tramelli, A., 2018. Anatomy of the campi flegrei caldera using enhanced seismic tomography models, *Scientific Reports,* **8**(1), 16254.

Chaves, C.A.M., Ritsema, J. & Koelemeijer, P., 2020. Comparing ray-theoretical and finite-frequency teleseismic traveltimes: implications for constraining the ratio of *S*-wave to *P*-wave velocity variations in the lower mantle, *Geophys. J. Int.,* **224**(3), 1540–1552.

Cobden, L., Zhuang, J., Lei, W., Wentzcovitch, R., Trampert, J. & Tromp, J., 2024. Full-waveform tomography reveals iron spin crossover in earth's lower mantle, *Nat. Commun.,* **15**(1), 1961.

Conder, J.A. & Wiens, D.A., 2006. Seismic structure beneath the Tonga arc and Lau back-arc basin determined from joint *V*p, *V*p/*V*s tomography, *Geochem. Geophys. Geosyst.,* **7**(3).

Conrad, C.P. & Lithgow-Bertelloni, C., 2006. Influence of continental roots and asthenosphere on plate-mantle coupling, *Geophys. Res. Lett.,* **33**(5).

Crossley, D.J., 1997. *Earth's Deep Interior,* Gordon and Breach.

Crotwell, H.P., Owens, T.J. & Ritsema, J., 1999. The TauP Toolkit: flexible seismic travel-time and ray-path utilities, *Seismol. Res. Lett.,* **70**(2), 154–160.

Davies, D.R., Goes, S. & Lau, H.C.P., 2015. Thermally dominated deep mantle LLSVPs: A review, in *The Earth's Heterogeneous Mantle: A Geophysical, Geodynamical, and Geochemical Perspective,* pp. 441–477, eds Khan, A. & Deschamps, F., Springer International Publishing.

Della Mora, S., Boschi, L., Tackley, P.J., Nakagawa, T. & Giardini, D., 2011. Low seismic resolution cannot explain *S*/*P* decorrelation in the lower mantle, *Geophys. Res. Lett.,* **38**(12).

Dhanoa, M., Sanderson, R., Shanmugalingam, S., López, S., Murray, J. & France, J., 2018. The distribution of the ratio of two correlated measured variables may not always be normal: Case studies related to meat quality and animal nutrition, *e-planet,* **16,** 43–50.

Dixon, W.J., 1950. Analysis of Extreme Values, *Ann. Math. Stat.,* **21**(4), 488–506.

Durand, S., Debayle, E., Ricard, Y., Zaroli, C. & Lambotte, S., 2017. Confirmation of a change in the global shear velocity pattern at around 1000 km depth, *J. geophys. Int.,* **211**(3), 1628–1639.

Eberhart-Phillips, D., 1990. Three-dimensional *P* and *S* velocity structure in the Coalinga region, California, *J. geophys. Res.: Solid Earth,* **95**(B10), 15 343–15 363.

Engdahl, E., van der Hilst, R. & Buland, R., 1998. Global teleseismic earthquake relocation with improved travel times and procedures for depth determination, *Bull. seism. Soc. Am.,* **88**(3), 722–743.

Engdahl, E., Di Giacomo, D., Sakarya, B., Gkarlaouni, C., Harris, J. & Storchak, D., 2020. ISC-EHB 1964-2016, an improved data set for studies of earth structure and global seismicity, *Earth Space Sci.,* **7**(1), e2019EA000897.

Ester, M., Krieger, H-P., Sander, J. & Xu,, X., 1996. A density-based algorithm for discovering clusters in large spatial databases with noise, in Pfitzner, D.W. & Salmon,, J.K., *KDD'96: Proceedings of the Second International Conference on Knowledge Discovery and Data Mining,* Vol. **96,** Association for Computing Machinery. pp. 226–231,

Fan, J. & Zhao, D., 2021. Subslab heterogeneity and giant megathrust earthquakes, *Nat. Geosci.,* **14**(5), 349–353.

Fang, H., Yao, H., Zhang, H., Thurber, C., Ben-Zion, Y. & van der Hilst, R.D., 2018. V_p/V_s tomography in the southern California plate boundary region using body and surface wave traveltime data, *J. geophys. Int.,* **216**(1), 609–620.

Fichtner, A. *et al.*, 2024. Seismic tomography 2024, *Bull. seism. Soc. Am.,* **114**(3), 1185–1213.

Freissler, R., Schuberth, B.S.A. & Zaroli, C., 2024. A concept for the global assessment of tomographic resolution and uncertainty, *Geophys. J. Int.,* **238**(2), 992–1012.

Gercek, H., 2007. Poisson's ratio values for rocks, *Int. J. Rock Mech. Mining Sci.,* **44**(1), 1–13.

Gerya, T.V., Connolly, J.A., Yuen, D.A., Gorczyk, W. & Capel, A.M., 2006. Seismic implications of mantle wedge plumes, *Phys. Earth planet. Inter.,* **156**(1–2), 59–74.

Gorbatov, A. & Kennett, B., 2003. Joint bulk-sound and shear tomography for western pacific subduction zones, *Earth planet. Sci. Lett.,* **210**(3–4), 527–543.

Hall, R. & Spakman, W., 2015. Mantle structure and tectonic history of SE Asia, *Tectonophysics,* **658,** 14–45.

Hamada, G.M., 2004. Reservoir fluids identification Using Vp/Vs Ratio?, *Oil Gas Sci. Technol. - Rev. IFP,* **59**(6), 649–654.

Hernlund, J.W. & Houser, C., 2008. On the statistical distribution of seismic velocities in earth's deep mantle, *Earth planet. Sci. Lett.,* **265**(3–4), 423–437.

Hinkley, D.V., 1969. On the ratio of two correlated normal random variables, *Biometrika,* **56**(3), 635–639.

Hosseini, K., Sigloch, K., Tsekhmistrenko, M., Zaheri, A., Nissen-Meyer, T. & Igel, H., 2019. Global mantle structure from multifrequency tomography using P, PP and P-diffracted waves, *Geophys. J. Int.,* **220**(1), 96–141.

Huang, Z., Zhao, D. & Wang, L., 2015. *P* wave tomography and anisotropy beneath southeast Asia: insight into mantle dynamics, *J. geophys. Res.: Solid Earth,* **120**(7), 5154–5174.

Hutchings, S.J. & Mooney, W.D., 2021. The seismicity of Indonesia and tectonic implications, *Geochem. Geophys. Geosyst.,* **22**(9), e2021GC009812.

Hyndman, R.D. & Peacock, S.M., 2003. Serpentinization of the forearc mantle, *Earth planet. Sci. Lett.,* **212**(3–4), 417–432.

International Seismological Centre, 2023a. On-line Bulletin.

International Seismological Centre, 2023b. ISC-EHB data set.

Karato, S.I., 1993. Importance of anelasticity in the interpretation of seismic tomography, *Geophys. Res. Lett.,* **20**(15), 1623–1626.

Karato, S.I., Forte, A., Liebermann, R., Masters, G. & Stixrude, L., 2000. Introduction. eds Karato,, S.I., Forte,, A., Liebermann,, R., Masters,, G. & Stixrude,, L.In *Earth's Deep Interior: Mineral Physics and Tomography From the Atomic to the Global Scale,* American Geophysical Union. 1–2.

Kennett, B.L.N., Engdahl, E.R. & Buland, R., 1995. Constraints on seismic velocities in the Earth from traveltimes, *Geophys. J. Int.,* **122**(1), 108–124.

Kennett, B.L.N., Widiyantoro, S. & van der Hilst, R.D., 1998. Joint seismic tomography for bulk sound and shear wave speed in the earth's mantle, *J. geophys. Res.: Solid Earth,* **103**(B6), 12469–12493.

Koelemeijer, P., Ritsema, J., Deuss, A. & van Heijst, H.J., 2015. SP12RTS: a degree-12 model of shear- and compressional-wave velocity for Earth's mantle, *Geophys. J. Int.,* **204**(2), 1024–1039.

Koelemeijer, P., Schuberth, B., Davies, D., Deuss, A. & Ritsema, J., 2018. Constraints on the presence of post-perovskite in earth's lowermost mantle from tomographic-geodynamic model comparisons, *Earth planet. Sci. Lett.,* **494,** 226–238.

Laske, G., Masters, G., Ma, Z. & Pasyanos, M., 2013. Update on CRUST1.0 - A 1-degree Global Model of Earth's Crust, in *Geophys. Res. Abstracts,* Abstract EGU2013–2658, 15.

Latallerie, F., Zaroli, C., Lambotte, S. & Maggi, A., 2022. Analysis of tomographic models using resolution and uncertainties: a surface wave example from the Pacific, *Geophys. J. Int.,* **230**(2), 893–907.

Latallerie, F., Zaroli, C., Lambotte, S., Maggi, A., Walker, A. & Koelemeijer, P., 2025. Towards surface wave tomography with 3D resolution and uncertainty, *Seismica,* **4**(1).

Lei, J. & Zhao, D., 2006. Global *P*-wave tomography: On the effect of various mantle and core phases, *Phys. Earth planet. Inter.,* **154**(1), 44–69.

Lennox, G.D., Dallimer, M. & Armsworth, P.R., 2012. Landowners' ability to leverage in negotiations over habitat conservation, *Theoret. Ecol.,* **5**(1), 115–128.

Leung, J., Walker, A.M., Koelemeijer, P., Restelli, F. & Davies, D.R., 2025. Quantitative assessment of tomographic proxies for lowermost mantle composition and mineralogy, *Phys. Earth planet. Inter.,* 107423. **368**.

Leys, C., Ley, C., Klein, O., Bernard, P. & Licata, L., 2013. Detecting outliers: do not use standard deviation around the mean, use absolute deviation around the median, *J. Exp. Social Psychol.,* **49**(4), 764–766.

Liu, T., Gong, J., Fan, W. & Lin, G., 2023. *In-situVp*/*Vs* reveals fault-zone material variation at the westernmost gofar transform fault, east pacific rise, *J. geophys. Res.: Solid Earth,* **128**(3), e2022JB025310.

Liu, Y., Suardi, I., Huang, X., Liu, S. & Tong, P., 2021. Seismic velocity and anisotropy tomography of southern Sumatra, *Phys. Earth planet. Inter.,* **316,** 106722.

Long, M.D. & Silver, P.G., 2008. The subduction zone flow field from seismic anisotropy: a global view, *Science,* **319**(5861), 315–318.

Lu, C., Grand, S.P., Lai, H. & Garnero, E.J., 2019. Tx2019slab: A new *P* and *S* tomography model incorporating subducting slabs, *J. geophys. Res.: Solid Earth,* **124**(11), 11 549–11 567.

Mag, A.M., Zaroli, C. & Koelemeijer, P., 2025. Bridging the gap between SOLA and deterministic linear inferences in the context of seismic tomography, *Geophys. J. Int.,* **242,** ggaf131.

Mahartha, D.S., Nugraha, A.D. & Sule, R.M.R., 2019. 3D *Vp*, *Vs*, and *Vp*/*Vs* microseismic tomography imaging on "MA" geothermal field: fluid saturation condition analysis, *J. Phys.: Conf. Ser.,* **1204**(1), 012090.

Masters, G., Laske, G., Bolton, H. & Dziewonski, A., 2000. The relative behavior of shear velocity, bulk sound speed, and compressional velocity in the mantle: Implications for chemical and thermal structure, in *Earth's Deep Interior: Mineral Physics and Tomography From the Atomic to the Global Scale,* pp. 63–87, ed. Karato, S.-I., Forte, A., Liebermann, R., Masters, G. & Stixrude, L., American Geophysical Union (AGU).

Matsushima, S., 1981. Compressional and shear wave velocities of igneous rocks and volcanic glasses to 900°c and 20 kbar, *Tectonophysics,* **75**(3–4), 257–271.

McNamara, A.K., 2019. A review of large low shear velocity provinces and ultra low velocity zones, *Tectonophysics,* **760,** 199–220.

Montelli, R., Nolet, G., Dahlen, F.A. & Masters, G., 2006. A catalogue of deep mantle plumes: New results from finite-frequency tomography, *Geochem. Geophys. Geosyst.,* **7**(11).

Morelli, A. & Dziewonski, A., 1987. Topography of the core–mantle boundary and lateral homogeneity of the liquid core, *Nature,* **325,** 678–683.

Mosca, I., Cobden, L., Deuss, A., Ritsema, J. & Trampert, J., 2012. Seismic and mineralogical structures of the lower mantle from probabilistic tomography, *J. geophys. Res.: Solid Earth,* **117**(B6), 1978–2012.

Müller, R.D., Sdrolias, M., Gaina, C. & Roest, W.R., 2008. Age, spreading rates, and spreading asymmetry of the world's ocean crust, *Geochem. Geophys. Geosyst.,* **9**(4).

Nasrabadi, A.T., Shirsavar, M.A., Ebrahimi, A. & Ghanbari, M., 2014. Investigating the PSNR calculation methods for video sequences with source

and channel distortions, in *2014 IEEE International Symposium on Broadband Multimedia Systems and Broadcasting,* pp. 1–4, IEEE.

Nelder, J.A. & Mead, R., 1965. A simplex method for function minimization, *Comput. J.,* **7**(4), 308–313.

Neumann van Padang, M. & Association, I.V., 1951. *Catalogue of the active volcanoes of the Indonesia,* Catalogue of the active volcanoes of the world, including solfatara fields; pt. 1, International Association of Volcanology, Napoli.

Nolet, G., 2008. *A Breviary of Seismic Tomography: Imaging the Interior of the Earth and Sun,* Cambridge Univ. Press.

Nolet, G., 2023. Path-averaged delay times for seismic tomography, *Geophys. J. Int.,* **235**(1), 996–1005.

Nolet, G. & van der Lee, S., 2022. Error estimates for seismic body wave delay times in the ISC-EHB Bulletin, *Geophys. J. Int.,* **231**(3), 1739–1749.

Nugraha, A.D., Indrastuti, N., Kusnandar, R., Gunawan, H., McCausland, W., Aulia, A.N. & Harlianti, U., 2019. Joint 3-D tomographic imaging of V_p, V_s and V_p/V_s and hypocenter relocation at Sinabung volcano, Indonesia from November to December 2013, *J. Volc. Geotherm. Res.,* **382,** 210–223.

Okabe, A., Kaneshima, S., Kanjo, K., Ohtaki, T. & Purwana, I., 2004. Surface wave tomography for southeastern Asia using IRIS-FARM and JISNET data, *Phys. Earth planet. Inter.,* **146**(1-2), 101–112.

Pijpers, F.P. & Thompson, M.J., 1992. Faster formulations of the optimally localized averages method for helioseismic inversions, *A&A (ISSN 0004-6361),* **262,** L33–L36.

Pijpers, F.P. & Thompson, M.J., 1993. Tests and Applications of the SOLA Inversion Method - a New Determination of the Solar Rotation Rate, in *GONG 1992. Seismic Investigation of the Sun and Stars, Vol. 42,* 241, ed. Brown, T.M., Astron. Soc. Pac.

Ramachandran, K. & Hyndman, R.D., 2012. The fate of fluids released from subducting slab in northern Cascadia, *Solid Earth,* **3**(1), 121–129.

Rawlinson, N., Fichtner, A., Sambridge, M. & Young, M.K., 2014. Chapter one - seismic tomography and the assessment of uncertainty , in *Advances in Geophysics, Vol. 55,* pp. 1–76, ed. Renata, D., Elsevier.

Resovsky, J. & Trampert, J., 2003. Using probabilistic seismic tomography to test mantle velocity–density relationships, *Earth planet. Sci. Lett.,* **215**(1-2), 121–134.

Restelli, F., Zaroli, C. & Koelemeijer, P., 2024. Robust estimates of the ratio between *S*- and *P*-wave velocity anomalies in the earth's mantle using normal modes, *Phys. Earth planet. Inter.,* **347,** 107135.

Reyners, M., Eberhart-Phillips, D., Stuart, G. & Nishimura, Y., 2006. Imaging subduction from the trench to 300 km depth beneath the central North Island, New Zealand, with V_p and V_p/V_s, *Geophys. J. Int.,* **165**(2), 565–583.

Ritsema, J. & Lekić, V., 2020. Heterogeneity of seismic wave velocity in earth's mantle, *Annu. Rev. Earth Planet. Sci.,* **48**(1), 377–401.

Romero, J. *et al.*, 2021. Volcanic lateral collapse processes in mafic arc edifices: a review of their driving processes, types and consequences, *Front. Earth Sci.,* **9**.

Rorabacher, D.B., 1991. Statistical treatment for rejection of deviant values: critical values of dixon's "q" parameter and related subrange ratios at the 95 per cent confidence level, *Anal. Chem.,* **63**(2), 139–146.

Rosalia, S., Widiyantoro, S., Nugraha, A.D. & Supendi, P., 2019. Double-difference tomography of *P*- and *S*-wave velocity structure beneath the western part of Java, Indonesia, *Earthq. Sci.,* **32**(1), 12–25.

Rost, S., 2013. Core–mantle boundary landscapes, *Nat. Geosci.,* **6**(2), 89–90.

Ruggieri, F., Fernández-Turiel, J.L., Saavedra, J., Gimeno, D., Polanco, E. & Naranjo, J.A., 2011. Environmental geochemistry of recent volcanic ashes from the southern Andes, *Environ. Chem.,* **8**(3), 236–247.

Shephard, G.E., Houser, C., Hernlund, J.W., Valencia-Cardona, J.J., Trønnes, R.G. & Wentzcovitch, R.M., 2021. Seismological expression of the iron spin crossover in ferropericlase in the earth's lower mantle, *Nat. Commun.,* **12**(1), 5905.

Silitonga, B., Suardi, I., Firmansyah, A., Hanif, M., Ramdhan, M. & Sembiring, A., 2023. Tectonic structure of northern Sumatra region based on seismic tomography of *P* and *S* wave velocity, *EKSPLORIUM,* **44**(1), 1–12.

Tesoniero, A., Auer, L., Boschi, L. & Cammarano, F., 2015. Hydration of marginal basins and compositional variations within the continental lithospheric mantle inferred from a new global model of shear and compressional velocity, *J. geophys. Res.: Solid Earth,* **120**(11), 7789–7813.

Tesoniero, A., Cammarano, F. & Boschi, L., 2016. S-to-p heterogeneity ratio in the lower mantle and thermo-chemical implications, *Geochem. Geophys. Geosyst.,* **17**(7), 2522–2538.

Tian, Y., Hung, S.H., Nolet, G., Montelli, R. & Dahlen, F., 2007. Dynamic ray tracing and traveltime corrections for global seismic tomography, *J. Comput. Phys.,* **226**(1), 672–687.

Toyokuni, G., Zhao, D. & Kurata, K., 2022. Whole-mantle tomography of southeast Asia: New insight into plumes and slabs, *J. geophys. Res.: Solid Earth,* **127**(11), e2022JB024298.

Trampert, J., Deschamps, F., Resovsky, J. & Yuen, D., 2004. Probabilistic tomography maps chemical heterogeneities throughout the lower mantle, *Science,* **306**(5697), 853–856.

Trautner, V.E. *et al.*, 2023. Compressibility of ferropericlase at high-temperature: Evidence for the iron spin crossover in seismic tomography, *Earth planet. Sci. Lett.,* **618,** 118296.

Tsampas, A., Scordilis, E., Papazachos, C. & Karakaisis, G., 2017. A homogeneous earthquake catalog of intermediate-deep focus global seismicity: completeness and spatio-temporal analysis, *Bull. Geol. Soc. Greece,* **50,** 3, 1270.

Walck, M.C., 1988. Three-dimensional vp /vs variations for the coso region, california, *J. geophys. Res.: Solid Earth,* **93**(B3), 2047–2052.

Wang, Z., Zhao, D., Chen, X. & Gao, R., 2022. Subducting slabs, Hainan plume and intraplate volcanism in SE Asia: insight from *P*-wave mantle tomography, *Tectonophysics,* **831,** 229329.

Wehner, D., Blom, N., Rawlinson, N., Daryono, Böhm, C., Miller, M.S., Supendi, P. & Widiyantoro, S., 2022. SASSY21: A 3-D seismic structural model of the lithosphere and underlying mantle beneath southeast Asia from multi-scale adjoint waveform tomography, *J. geophys. Res.: Solid Earth,* **127**(3), e2021JB022930.

Weston, J., Engdahl, E., Harris, J., Di Giacomo, D. & Storchak, D., 2018. ISC-EHB: Reconstruction of a robust earthquake data set, *Geophys. J. Int.,* **214**(1), 474–484.

Widiyantoro, S., Pesicek, J.D. & Thurber, C.H., 2011. Subducting slab structure below the eastern Sunda arc inferred from non-linear seismic tomographic imaging, *Geol. Soc. London Special Publ.,* **355**(1), 139–155.

Xie, F., Wang, Z., Zhao, D., Gao, R. & Chen, X., 2023. Seismic imaging of the java subduction zone: New insight into arc volcanism and seismogenesis, *Tectonophysics,* **854,** 229810.

Zaroli, C., 2016. Global seismic tomography using Backus–Gilbert inversion, *Geophys. J. Int.,* **207**(2), 876–888.

Zaroli, C., 2019. Seismic tomography using parameter-free Backus–Gilbert inversion, *Geophys. J. Int.,* **218**(1), 619–630.

Zaroli, C., Koelemeijer, P. & Lambotte, S., 2017. Toward seeing the earth's interior through unbiased tomographic lenses, *Geophys. Res. Lett.,* **44**(22), 11 399–11 408.

Zenonos, A., De Siena, L., Widiyantoro, S. & Rawlinson, N., 2019. *P* and *S* wave travel time tomography of the SE Asia-Australia Collision Zone, *Phys. Earth planet. Inter.,* **293,** 106267.

Zenonos, A., De Siena, L., Widiyantoro, S. & Rawlinson, N., 2020. Direct inversion of *S-P* differential arrival times for ratio in SE Asia, *J. geophys. Res.: Solid Earth,* **125**(5), e2019JB019152.